


Neural network based rate- and temperature-dependent Hosford-Coulomb fracture initiation model

Journal Article**Author(s):**

Li, Xueyang; Roth, Christian ; Mohr, Dirk

Publication date:

2023-12-15

Permanent link:

<https://doi.org/10.3929/ethz-b-000629349>

Rights / license:

[Creative Commons Attribution 4.0 International](#)

Originally published in:

International Journal of Mechanical Sciences 260, <https://doi.org/10.1016/j.ijmecsci.2023.108643>



Neural network based rate- and temperature-dependent Hosford–Coulomb fracture initiation model

Xueyang Li^a, Christian C. Roth^a, Dirk Mohr^{a,b,*}

^a Chair of Artificial Intelligence in Mechanics and Manufacturing, Department of Mechanical and Process Engineering, ETH Zurich, Zurich, Switzerland

^b Impact and Crashworthiness Lab, Department of Mechanical Engineering, Massachusetts Institute of Technology, Cambridge, MA, USA

ARTICLE INFO

Keywords:

- A. Machine learning
- B. Rate- and temperature effect
- C. Finite element analysis
- D. Ductile fracture

ABSTRACT

The accurate description of the strain rate and temperature dependent response of metals is a perpetual quest in crashworthiness and forming applications. In the present study, experiments are carried out to probe the onset of ductile fracture for an aluminum alloy AA7075-T6 for 136 combinations of stress state, strain rate and temperature. The experimental campaign covers strain rates ranging from 0.001/s to 100/s, and temperatures ranging from 20 °C to 360 °C. We combine a YLD2000 yield surface with a neural network based hardening law to describe the large deformation plasticity response of the material. The NN-based hardening law is trained on experimental data, achieving 3.9% accuracy on force predictions including the post-necking regime. The loading paths to fracture are extracted for each simulation, showcasing non-proportionally evolving stress triaxiality, Lode angle parameter, strain rate and temperature. A neural network parameterized Hosford–Coulomb fracture locus is proposed, which is trainable using these evolving loading histories. The accuracy of the proposed fracture model is validated against the experimental onset of fracture, predicting the fracture onset at an error of 8%.

1. Introduction

The effect of the stress state and loading path changes on ductile failure has been extensively studied through experiments (e.g. [1–8]) and micromechanical analysis (e.g. [9–14]). The rate of void growth is monotonically related to stress triaxiality (e.g. [15,16]) which is an important qualitative feature that is well captured by most porous plasticity models (e.g. [17–19]). In addition to the effect of the stress triaxiality, the fracture strains are affected by the Lode angle parameter in a non-monotonic manner, as observed in studies by Bai and Wierzbicki [20], Lou and Huh [21], Lou et al. [22], Mohr and Marcadet [23], Xiao et al. [24]. Furthermore, the fracture strains are affected by material anisotropy (e.g. [25–27]). And finally, the ductility is affected by the temperature and strain rate (e.g. [28,29]), but experimental data is still scarce mostly due to the high experimental complexity and the wide range of failure mechanisms that can become active under these conditions (e.g. [30]).

In engineering applications involving the viscoplastic behavior of metals, the phenomenological Johnson-Cook plasticity model [31] is widely used. Despite the missing explicit incorporation of the underlying physical mechanisms governing the strain rate and

temperature-dependent fracture response, this model has been remarkably successful over the past three decades due to its simplicity and ease of parameter identification. Several extensions of the Johnson-Cook plasticity model have also been proposed and compared (e.g. [32–38]). As an alternative, physics-based thermo-visco-plastic models (e.g. [39–47]) have been developed mostly based on the theory of thermally-activated dislocation motion (e.g. [48,49]). These models aim to capture the underlying physics of dislocation motion under different loading conditions, but they often require more complex calibration procedures and are computationally more demanding as compared to purely phenomenological models.

Higher fracture strains at higher strain rates are observed in dual phase steels (e.g. [35,47]), while a reduction in formability at higher strain rates have been reported for aluminum alloys (e.g. [50,51]). Additionally, the effect of temperature adds another complexity to ductile fracture of metals in the form of twinning (e.g. [52]), phase transformation (e.g. [53]), or dynamic strain aging (e.g. [54]). Among the stress-state dependent phenomenological fracture models, the Johnson-Cook model and its modifications (e.g. [34]) as well as the Hosford–Coulomb model (e.g. [35]) incorporate the strain rate and temperature effects on ductile fracture (e.g. [55,56]).

* Corresponding author at: Chair of Artificial Intelligence in Mechanics and Manufacturing, Department of Mechanical and Process Engineering, ETH Zurich, Zurich, Switzerland.

E-mail address: mohr@mit.edu (D. Mohr).

<https://doi.org/10.1016/j.ijmecsci.2023.108643>

Received 3 April 2023; Received in revised form 5 July 2023; Accepted 20 July 2023

Available online 21 July 2023

0020-7403/© 2023 The Authors. Published by Elsevier Ltd. This is an open access article under the CC BY license (<http://creativecommons.org/licenses/by/4.0/>).

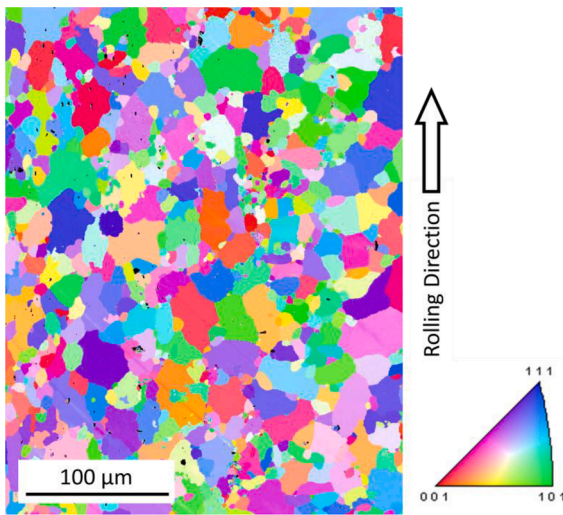


Fig. 1. EBSD inverse pole map of the AA7075-T6 base material with a mean grain diameter of 12 μm (min. 5 μm , max. 30 μm).

While machine learning based constitutive models can be built such as to replace the entire mathematical framework of conventional constitutive models (e.g. [57,58]), the targeted insertion of neural network functions into existing phenomenological and physics-based plasticity and fracture models has also been pursued. Fully connected neural networks represent the relationship between the input vector \mathbf{x} (with N_{IN} entries) and the output vector \mathbf{y} (with N_{OUT} entries). It is described through a series of nonlinear transformations. Each of these transformation computes a new vector $\mathbf{H}^{(n+1)}$ (hidden layer) based on the output $\mathbf{H}^{(n)}$ of the previous transformation,

$$\mathbf{x} \rightarrow \mathbf{H}^{(1)} \rightarrow \mathbf{H}^{(2)} \rightarrow \dots \rightarrow \mathbf{H}^{(N_{HL})} \rightarrow \mathbf{y} \quad (1)$$

with

$$\mathbf{H}^{(n+1)} = g(\mathbf{W}^n \mathbf{H}^n + \mathbf{b}^{n+1}) \quad (2)$$

where $g(\cdot)$ is a non-linear activation function. The trainable parameters of the network are the weight matrices \mathbf{W}^n and the bias vectors \mathbf{b}^{n+1} . The network architecture is then characterized by the hyper-parameters N_{HL} (the number of hidden layers), N_{NPL} (number of neurons per hidden layer) and the specific choice of the activation function. Al-Haik et al. [59] made use of a fully-connected neural network (FCNNs) to predict the one-dimensional stress relaxation of a polymer matrix carbon-fiber composite material using the temperature, initial stress and time as input and the relaxation stress as output. Talebi-Ghadikolaei et al. [60] used a machine learning model to predict damage evolution during the bending process of the aluminum 6061-T6 sheet metal. Kessler et al. [61] employed an FCNN to describe the rate- and temperature-dependent stress-strain response of an aluminum 6061 alloy. A similar FCNN approach has been taken by Jenab et al. [62] to model the rate-dependent hardening response of an aluminum 5182-O alloy. Jordan et al. [63] demonstrated that neural network-based models are able to learn the rate- and temperature-dependent hardening response from robot-assisted high-throughput experiments without imposing the constraint of constant temperature or strain rate conditions. Li et al. [64] introduced a neural network based hardening law to account for complex phenomena such as a non-monotonic yield stress-dependence on the temperature. Furthermore, a counter-example trained neural network is proposed [65] to separate between positive rate effects associated with viscous flow and negative rate effects associated with dynamic strain aging.

In close analogy with the enhancement of phenomenological plasticity models, the accuracy of ductile fracture models may also be

improved through the introduction of neural network functions. With that goal in mind, Pandya et al. [66] used a neural network to describe the fracture locus as a function of triaxiality, Lode angle parameter, strain rate and temperature. However, their flexible model has a drawback: it is trained using calibrated Hosford-Coulomb fracture models assuming constant, i.e. non-evolving strain rates and temperatures. Similar to the evolution in stress state during loading of a material point, the significant increase in temperature (>20 $^{\circ}\text{C}$ for aluminum and >150 $^{\circ}\text{C}$ for steel) and rise in strain rate (up to an order of magnitude) occurring at elevated loading speeds ($> 1/\text{s}$) needs to be taken into account (e.g. [67]). Averaging or assuming constant values can lead to inaccurate predictions of the fracture strains.

In the present work, a neural network enriched fracture model is developed to address the shortcomings of the approach taken by Pandya et al. [66]. Aluminum 7075 is chosen for the associated experimental campaign due to the important effects of temperature and strain rate during hot stamping (e.g. [68-70]). This experimental campaign investigates a total of 136 unique combinations of stress states (uniaxial tension, notched tension, central hole and shear specimens), strain rates (from 0.001/s to 100/s) and temperatures (from 20 $^{\circ}\text{C}$ to 360 $^{\circ}\text{C}$). A YLD2000-3D yield surface combined with a neural network based hardening model is employed to accurately describe the plasticity response at large deformation. The loading paths to fracture reveal significant evolutions in triaxiality, Lode angle parameter, strain rate and temperature. A neural network parameterized Hosford-Coulomb (HC) fracture model is proposed to accurately map the evolution in material ductility. The HC formulation constrains the model's behavior in triaxiality and Lode space, while the network retains its flexibility in the rate- and temperature domain. The fracture model is calibrated using the complete loading histories while minimizing the loss on the terminal damage. The network predictions are compared to the experimental onset of fracture using full loading paths.

2. Material and experimental procedures

This section details the base material, specimen design and experimental campaign involved in the study. Firstly, an electron back-scattered diffraction (EBSD) analysis is carried out to reveal the initial texture of the base material. The specimen design is subsequently described. The experimental procedure at various combinations of strain rates, temperatures and stress states are then described, together with the corresponding measurement and acquisition devices.

2.1. Material and specimens

The material under investigation is an aluminum alloy AA7075-T6 which had been received in the form of 2 mm thick sheets. An electron back-scattered diffraction (EBSD) analysis (Fig. 1) reveals the polycrystalline microstructure. The estimated average grain area is 148 μm^2 (following the ASTM E112-12 planimetric method [71]), with a mean grain diameter of approximately 12 μm . The grain size varies from 5 μm to 30 μm , with intermetallic particles located both inside the grain and along the grain boundaries.

All specimens are extracted using water-jet cutting, with the exception of the SH specimens. The latter are extracted using wire-electric discharge machining to obtain a lower roughness of the machined edges. The following specimen geometries are considered:

- Uniaxial tension (UT) specimens with a 40 mm long and 10 mm wide gauge section (Fig. 2a). A reduced gauge section (15 mm length and 5 mm width) is used for dynamic UT specimens (Fig. 2g).
- Central hole (CH) specimens with a circular cut-out of 5 mm or 8 mm diameter. The water-jet pre-cut hole is reamed to obtain a high surface quality of the hole (Fig. 2b).
- Notched tension (NT) specimens with symmetric lateral cutouts of radius $R = 20$ mm and $R = 6$ mm (Fig. 2c-d). Identical gauge section

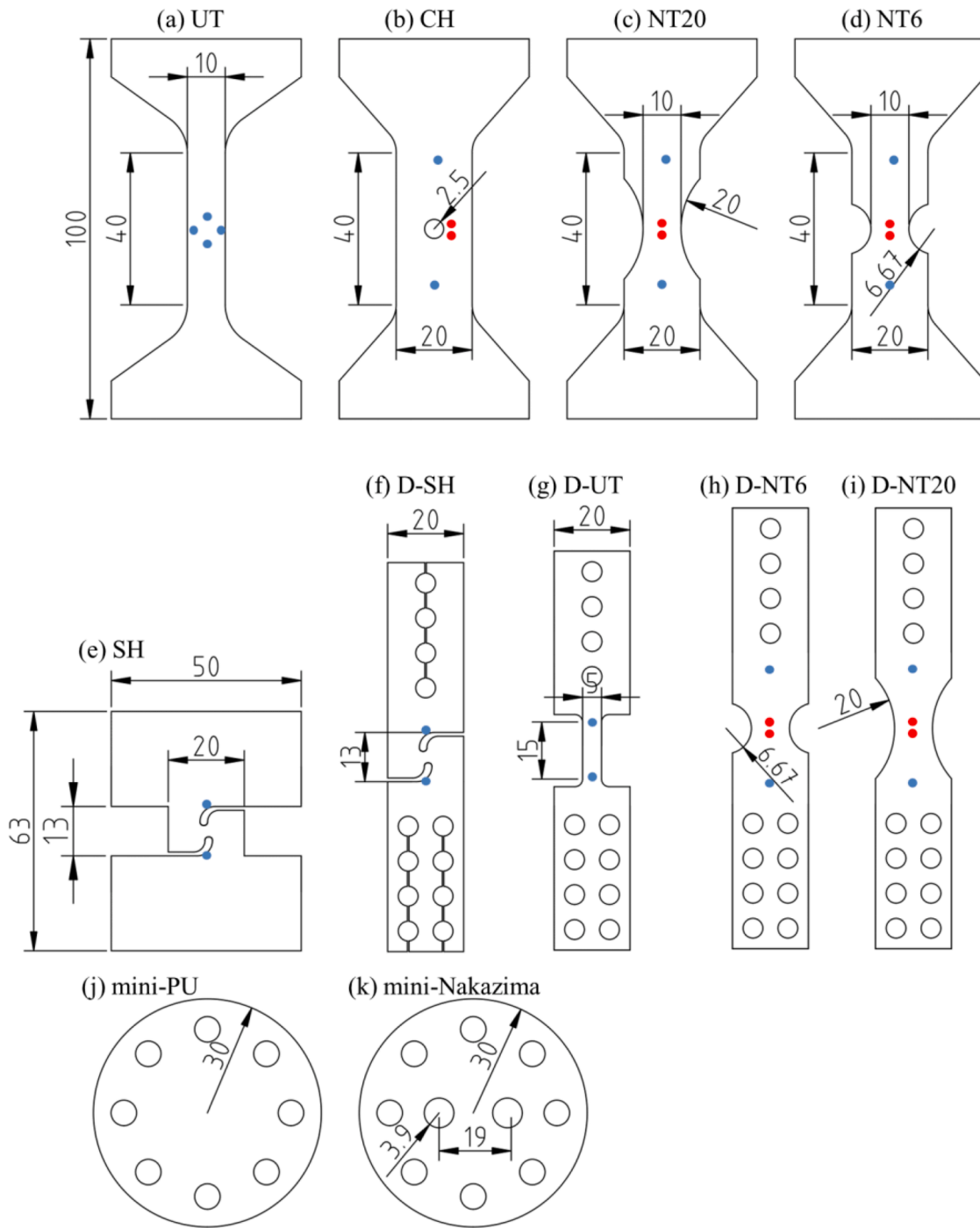


Fig. 2. Specimen geometries used for material characterization: (a) uniaxial tension, (b) central hole, (c) notched tension with $R = 20$ mm cutout, (d) notched tension with $R = 6$ mm cutout, (e) shear, (f) dynamic shear, (g) dynamic uniaxial tension, (h) dynamic NT6, (i) dynamic NT20, (j) mini-Punch and (k) mini-Nakazima specimens. The blue dots represent the location of the virtual extensometers used to measure relative displacement and speed. The red dots highlight the corresponding locations at which axial surface strains are extracted with DIC. The Lankford ratios are measured from a horizontal and vertical pair of virtual extensometers (blue dots) on the UT specimens.

designs are used with modified clamping fixtures on the universal testing machine (NT) and the split Hopkinson bar system (D-NT, Fig. 2h–i).

- In-plane shear (SH) specimens with a single gauge section designed for medium ductility materials (Roth and Mohr, 2018) (Fig. 2e). Fig. 2f shows the dynamic shear (D-SH) specimens for use in the Split-Hopkinson bar fixture.
- Mini-punch [3] specimens for equi-biaxial tension tests (Fig. 2j).

- Mini-Nakazima [72] specimens for plane-strain tension tests (Fig. 2k).

2.2. Experimental procedures

2.2.1. Experimental techniques for low strain rates

All experiments at low strain rates are carried out on a 100 kN hydraulic universal testing machine (Instron 8801) using a constant crosshead velocity. An overview of the experimental setup is provided in

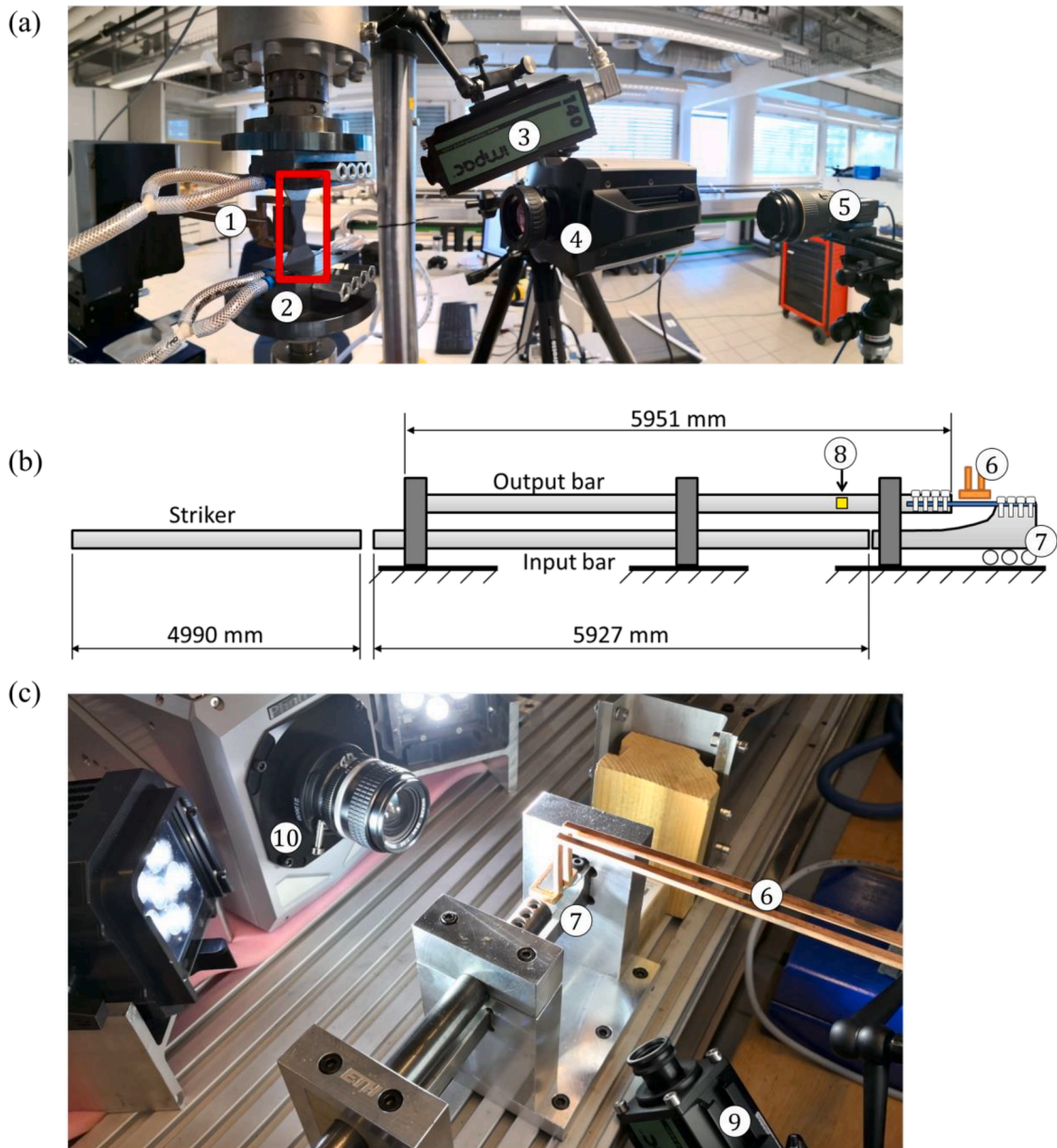


Fig. 3. (a) High temperature experimental setup at low and intermediate speeds with ①customized induction heating coil, ②NT20 specimen in water-cooled clamps, ③pyrometer, ④infrared (high speed) camera, ⑤optical camera. (b) Schematic drawing of the split Hopkinson pressure bar system for tensile test with ⑥customized induction heating coil, ⑦load-inversion device and ⑧strain gauge attached to the output bar. (c) Picture of the high speed – high temperature experimental setup: ⑥pyrometer and ⑩high-speed optical camera.

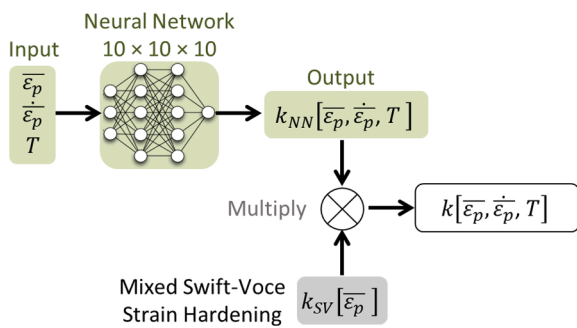


Fig. 4. Schematic diagram of the neural network based strain, strain rate and temperature dependent hardening function.

Table 1

The mean AA7075 material parameters extracted from quasi-static tensile tests: yield stress σ_{YS} , the ultimate tensile strength σ_{UTS} , the engineering strains at ultimate tensile strength ϵ_U , the engineering strain to fracture ϵ_T and Lankford ratios r_α .

α [°]	σ_{YS} [MPa]	σ_{UTS} [MPa]	ϵ_U [-]	ϵ_T [-]	r_α [-]
0	468	562	0.13	0.15	0.57
15	466	561	0.12	0.17	0.64
30	460	559	0.13	0.14	0.86
45	451	547	0.13	0.16	1.07
60	442	542	0.12	0.13	0.98
75	460	558	0.13	0.15	0.82
90	462	559	0.12	0.13	0.82

Table 2
Plasticity model parameters for AA7075 calibrated from room temperature low speed experiments.

E [GPa]	ν [-]	ρ [kg/m ³]	C_p [J/kgK]	η_k [-]	k_{cond} [W/mK]			
69	0.3	2780	897	0.9	130			
A [MPa]	ϵ_0 [-]	n [-]	k_0 [MPa]	Q [MPa]	β [-]	α [-]		
855.4	0.026	0.151	502.4	194.1	10.1	0.50		
α_1	α_2	α_3	α_4	α_5	α_6	α_7	α_8	
0.899	1.039	0.998	1.007	1.017	0.952	1.030	1.052	

Fig. 3a. The uniaxial tension (UT) specimens are tested at an actuator speed of 2.4 mm/min (4×10^{-5} m/s), corresponding to an engineering strain rate of 0.001/s. To obtain similar strain rates, the notched tension (NT), central hole (CH) and in-plane shear (SH) specimens are tested at a speed of 0.4 mm/min (6.6×10^{-6} m/s), while mini-Nakazima and mini-punch specimens are tested at 2 mm/min (3.3×10^{-5} m/s). A random

graphite-based black and white speckle pattern (speckle diameter of about 140 μm) is applied to the specimens prior to testing. Using an induction heating system with specimen specific induction coil shapes, all specimens are heated to their respective target temperatures between 20 °C and 360 °C at a rate of about 30 K/s [65]. For low speed tests, isothermal conditions are assured with a closed-loop feedback control of the induction heating system with a pyrometer measuring the surface temperature at a frequency of about 120 Hz. A 12 Megapixel digital camera (FLIR, Model GS3-U3-120S6M-C) with a 100 mm f2.8 macro lens is utilized to acquire images at a frame rate of 1 Hz. Digital image correlation (DIC) is performed using VIC-2D software (version 4.4.1, Correlated Solutions) with a virtual strain gage length of 0.37 mm [29]. This results in a spatial resolution of 13 $\mu\text{m}/\text{pixel}$ for the SH and 25 $\mu\text{m}/\text{pixel}$ for all other specimens. A FLIR x6801sc high speed infrared camera is employed at 1 Hz to monitor the temperature evolution on the specimen surface in the area of interest, achieving a spatial resolution of 340 $\mu\text{m}/\text{pixel}$.

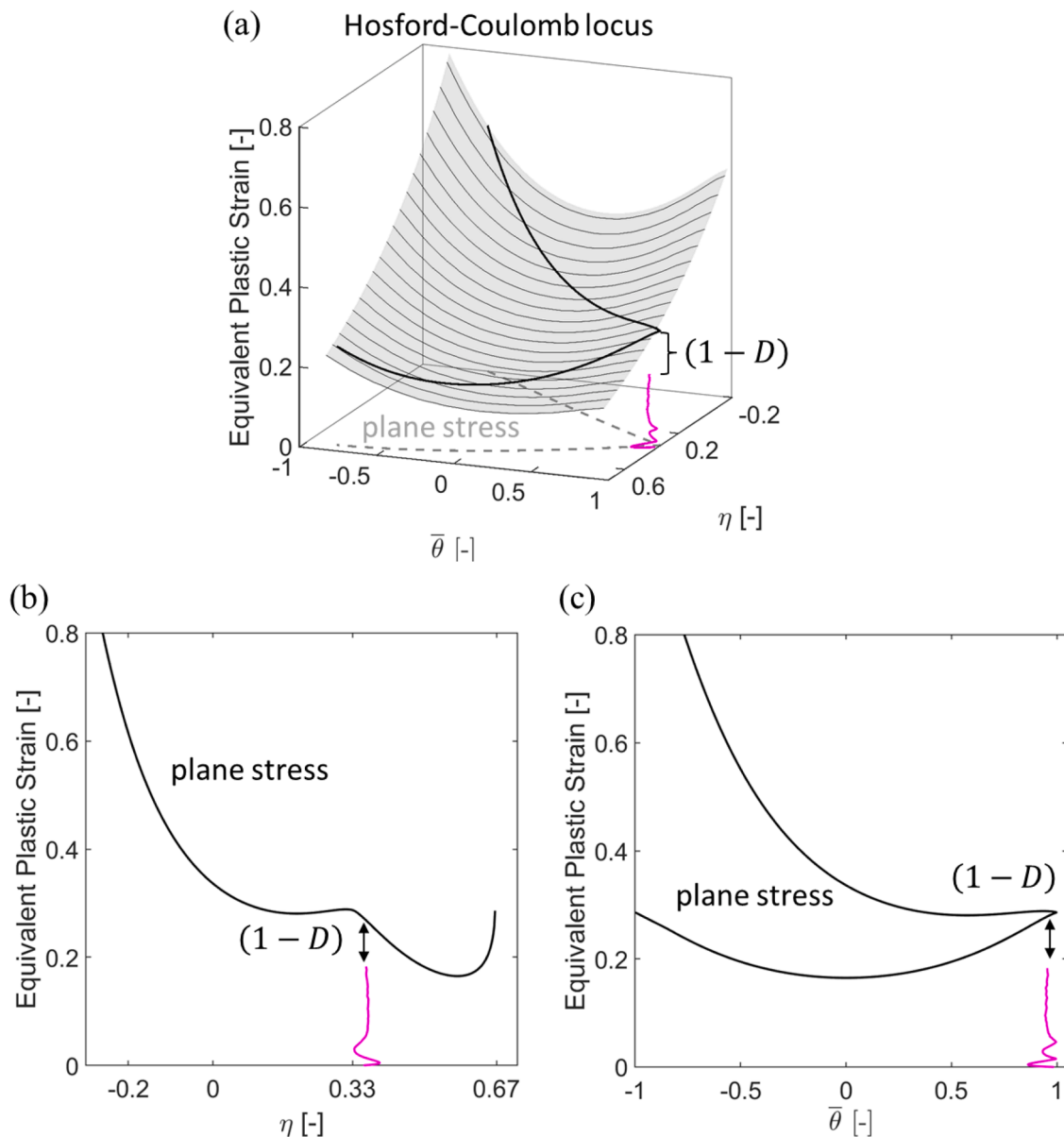


Fig. 5. Hosford–Coulomb fracture initiation model: (a) Fracture surface from quasi-static experiments at 20 °C. For plane stress conditions, the HC criterion is visualized in (b) the equivalent plastic strain versus triaxiality plane and (c) the equivalent plastic strain versus Lode angle parameter plane.

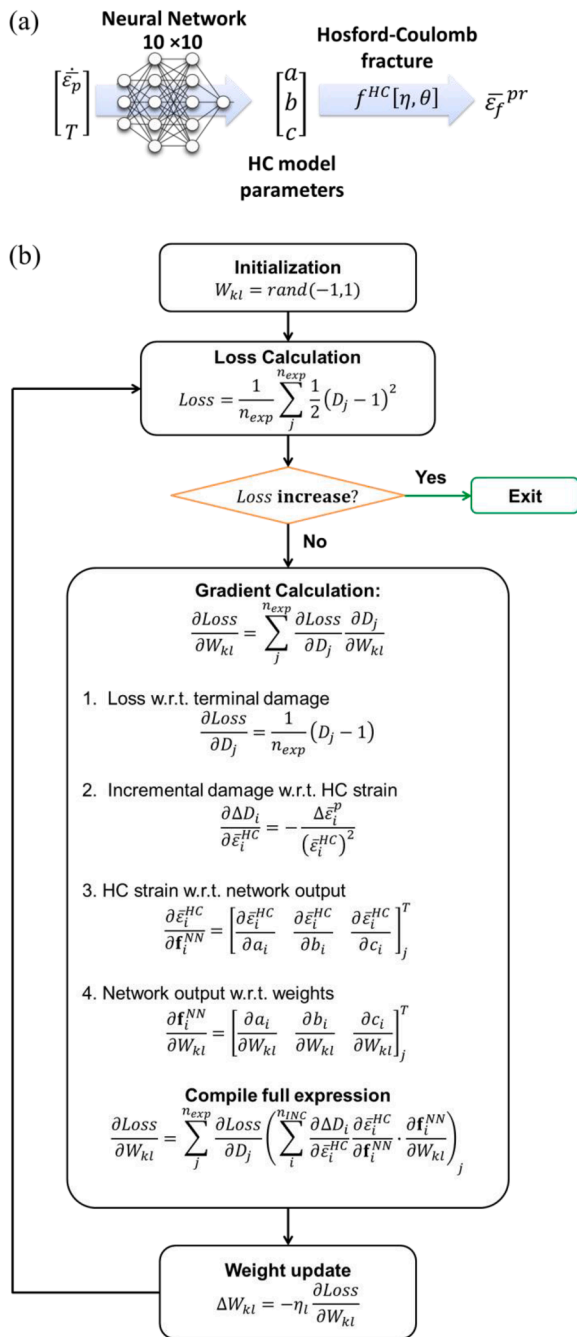


Fig. 6. (a) Schematic diagram for the neural network parameterized HC fracture model. (b) Training procedure for the NN parameterized HC fracture model.

2.2.2. Experimental techniques for intermediate strain rates

Intermediate strain rate experiments are carried out at 0.1/s and 2/s, corresponding to 240 mm/min (4×10^{-3} m/s) and 4800 mm/min (0.08 m/s) for UT tests. To obtain comparable strain rates, the notched tension (NT), central hole (CH) and in-plane shear (SH) tests are performed at 40 mm/min (6.6×10^{-4} m/s) and 800 mm/min (1.3×10^{-2} m/s). For all intermediate strain rate tests, an optical high-speed camera (Photron SA-Z) is employed to obtain DIC images at 1000 Hz and 8000 Hz, respectively. This setup achieves a spatial resolution of 58 $\mu\text{m}/\text{pixel}$. The infrared camera (FLIR x6801sc) monitors the temperature evolution on

the specimen surface at 2000 Hz with a resolution of 640×64 pixels. We trigger the fully synchronized data and image acquisition simultaneously with the rise in the analog force signal.

2.2.3. Experimental techniques for high strain rates

Experiments at high strain rates are performed on a modified split Hopkinson pressure bar system. Fig. 3b and c summarize the high speed-high temperature experimental setup. The system features a 4990 mm long striker, a 5927 mm long input bar and a 5951 mm output bar. A load inversion device converts the compressive loading into tensile loading at the specimen level [28]. The specimen specific custom-made induction coils heat the flat specimens from the top. The optical high-speed camera operates at 100 kHz, monitoring the global displacement on the specimen shoulder from the side [65]. With a resolution of 512×280 pixels, this setup achieves a spatial resolution of 71 $\mu\text{m}/\text{pixel}$. The axial force histories are calculated from strain gauge signals on the output bar.

$$F_{out}[t] = E_{out} A_{out} \epsilon_{tra}[t]. \quad (3)$$

A laser light barrier is mounted right before the striker impacts the input bar, simultaneously triggering the image and data acquisition and turning off the induction system to avoid any electro-magnetic interference on the strain gauge signals.

3. Plasticity modeling

Accurate predictions of the large-deformation, post-necking plastic response of the material is critical for identifying loading paths to fracture. This section starts by introducing a novel combination of the analytical YLD2000-3D model [73] with a neural-network based hardening function, to account for the material's combined rate- and temperature dependency. Procedures to calibrate this modeling framework is then summarized.

3.1. Yield function and hardening law

In the present work, we make use of the 3D extension by Dunand et al. [73,74] of the YLD2000-2d model [75]. The yield function is defined by the equivalent stress and a flow resistance,

$$f = \bar{\sigma}_{Yld2000} - k[\bar{\epsilon}_p, \dot{\bar{\epsilon}}_p, T], \quad (4)$$

with

$$\bar{\sigma}_{Yld2000} = \frac{1}{2^{1/m}} (\phi[s'] + \phi[s''])^{1/m}. \quad (5)$$

The equivalent stress is a function of the two deviatoric stress vectors s' and s'' , which are calculated from the Cauchy stress vector $\sigma = \{\sigma_{xx}, \sigma_{yy}, \sigma_{zz}, \sigma_{xy}, \sigma_{yz}, \sigma_{zx}\}$

$$s' = \{s'_{xx}, s'_{yy}, s'_{xy}, s'_{yz}, s'_{xz}\} \text{ and } s'' = \{s''_{xx}, s''_{yy}, s''_{xy}, s''_{yz}, s''_{xz}\}. \quad (6)$$

In close analogy to the original Yld2000-2d, we calculate the stress deviatoric vectors s' and s'' through linear transformations

$$s' = L' \sigma \text{ and } s'' = L'' \sigma. \quad (7)$$

The linear transformations L' and L'' are described using eight Yld2000-2D parameters $\alpha_1, \dots, \alpha_8$ and the exponent $m = 8$.

$$L' = \frac{1}{3} \begin{bmatrix} 2\alpha_1 & -\alpha_1 & -\alpha_1 & 0 & 0 & 0 \\ -\alpha_2 & 2\alpha_2 & -\alpha_2 & 0 & 0 & 0 \\ 0 & 0 & 0 & 3\alpha_7 & 0 & 0 \\ 0 & 0 & 0 & 0 & 3 & 0 \\ 0 & 0 & 0 & 0 & 0 & 3 \end{bmatrix} \quad (8)$$

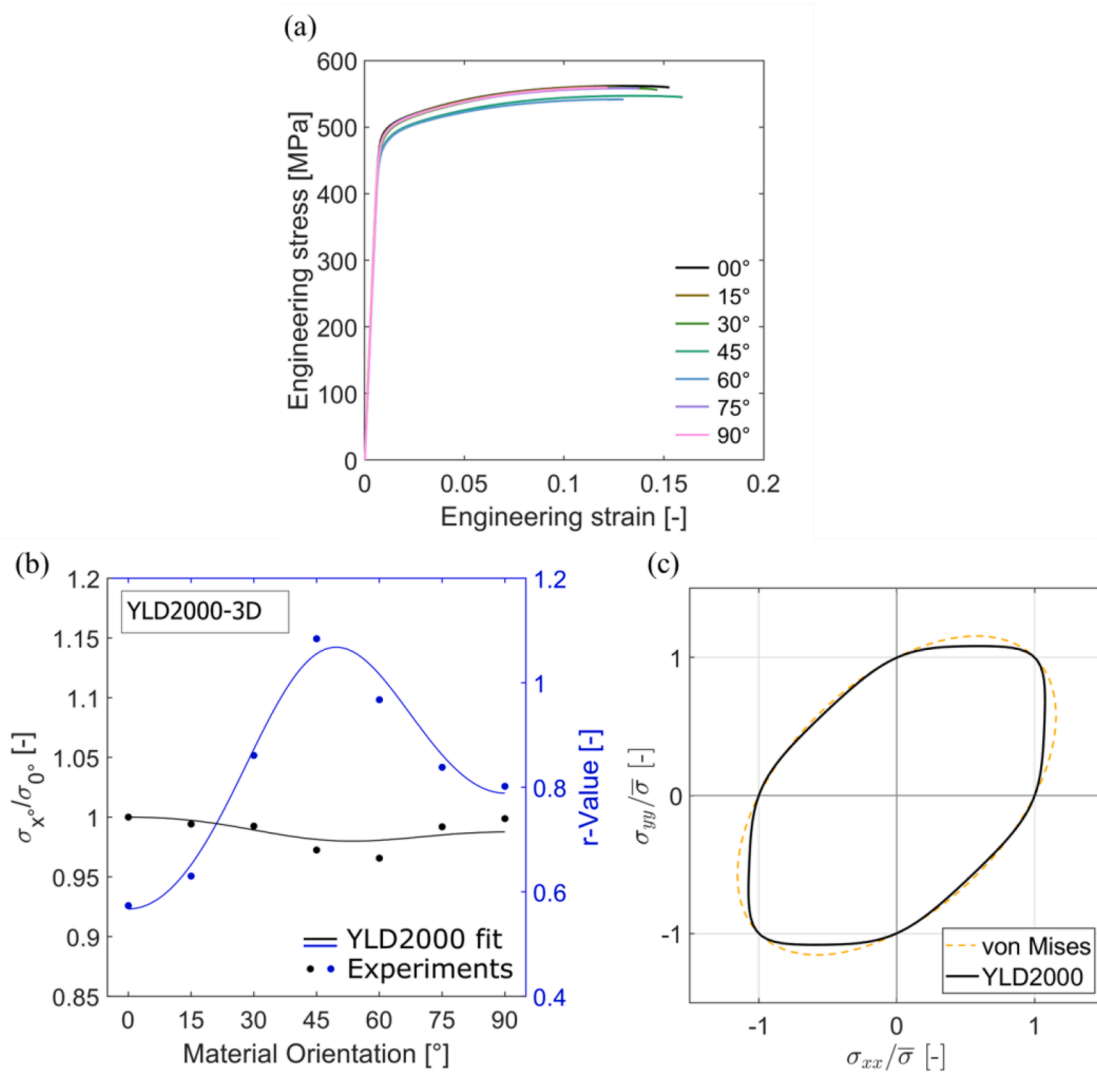


Fig. 7. (a) Engineering stress–strain curve from uniaxial tensile tests of seven orientations (0°, 15°, ..., 90°). (b) Yield stress ratios (black) and Lankford ratios (blue) as a function of material orientation together with model fit. The experimental measurements are denoted by dots. (c) Yield locus for plane stress state (black line) compared to von Mises yield surface (yellow line). (For interpretation of the references to colour in this figure legend, the reader is referred to the web version of this article.).

$$\frac{1}{9} \begin{bmatrix} -2\alpha_3 + 2\alpha_4 + 8\alpha_5 - 2\alpha_6 & -4\alpha_4 + 4\alpha_6 + \alpha_3 - 4\alpha_5 & \alpha_3 + 2\alpha_4 - 4\alpha_5 - 2\alpha_6 & 0 & 0 & 0 \\ 4\alpha_3 - 4\alpha_4 - 4\alpha_5 + \alpha_6 & -2\alpha_3 + 8\alpha_4 + 2\alpha_5 - 2\alpha_6 & -2\alpha_3 - 4\alpha_4 + 2\alpha_5 + \alpha_6 & 0 & 0 & 0 \\ 0 & 0 & 0 & 9\alpha_8 & 0 & 0 \\ 0 & 0 & 0 & 0 & 9 & 0 \\ 0 & 0 & 0 & 0 & 0 & 9 \end{bmatrix} \quad (9)$$

The functions ϕ' and ϕ'' are the modified Yld2000-2d functions that extends into the general stress states.

$$\phi'[s'] = \left[(s'_{xx} - s'_{yy})^2 + 4(s'^2_{xy} + s'^2_{xz} + s'^2_{yz}) \right]^{\frac{m}{2}} \quad (10)$$

$$\begin{aligned} \phi''[s''] &= \left[\frac{3}{2}(s''_{xx} + s''_{yy}) + \frac{1}{2}\sqrt{(s''_{xx} - s''_{yy})^2 + 4(s''^2_{xy} + s''^2_{xz} + s''^2_{yz})} \right]^m \\ &+ \left[\frac{3}{2}(s''_{xx} + s''_{yy}) - \frac{1}{2}\sqrt{(s''_{xx} - s''_{yy})^2 + 4(s''^2_{xy} + s''^2_{xz} + s''^2_{yz})} \right]^m \end{aligned} \quad (11)$$

In the case of plane stress, the above functions reduce to the Yld2000-2d function.

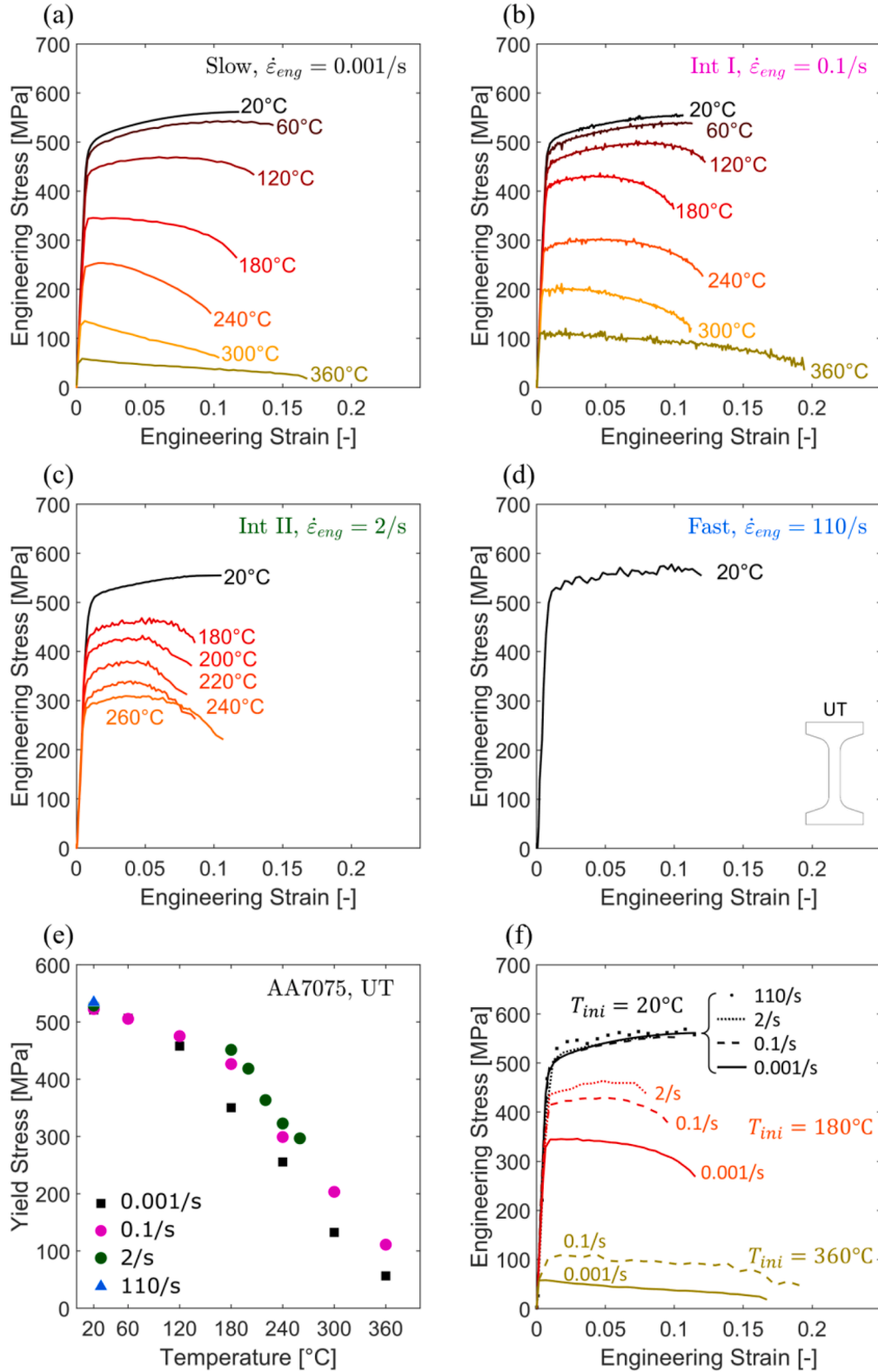


Fig. 8. Engineering stress–strain curves of uniaxial tensile experiments obtained at nominal strain rates of (a) 0.001/s, (b) 0.1/s, (c) 2/s and (d) 110/s for various temperatures. (e) Extracted 0.2% yield stress as a function of temperature for all strain rates. (f) Engineering stress–strain curves for initial temperatures of 20 °C, 180 °C and 360°C.

An associated flow rule is employed herein and the equivalent plastic strain increment $d\bar{\epsilon}_p$ is retrieved through work conjugacy

$$\boldsymbol{\sigma} : d\boldsymbol{\epsilon}_p = \bar{\sigma}_{Y1d2000} d\bar{\epsilon}_p. \quad (12)$$

As proposed by Li et al. [64], we decompose the deformation resistance k into a reference strain hardening term $k_{SV}[\bar{\epsilon}_p]$ and a neural network term $k_{NN}[\bar{\epsilon}_p, \dot{\bar{\epsilon}}_p, T]$ accounting for the effect of strain rate and temperature,

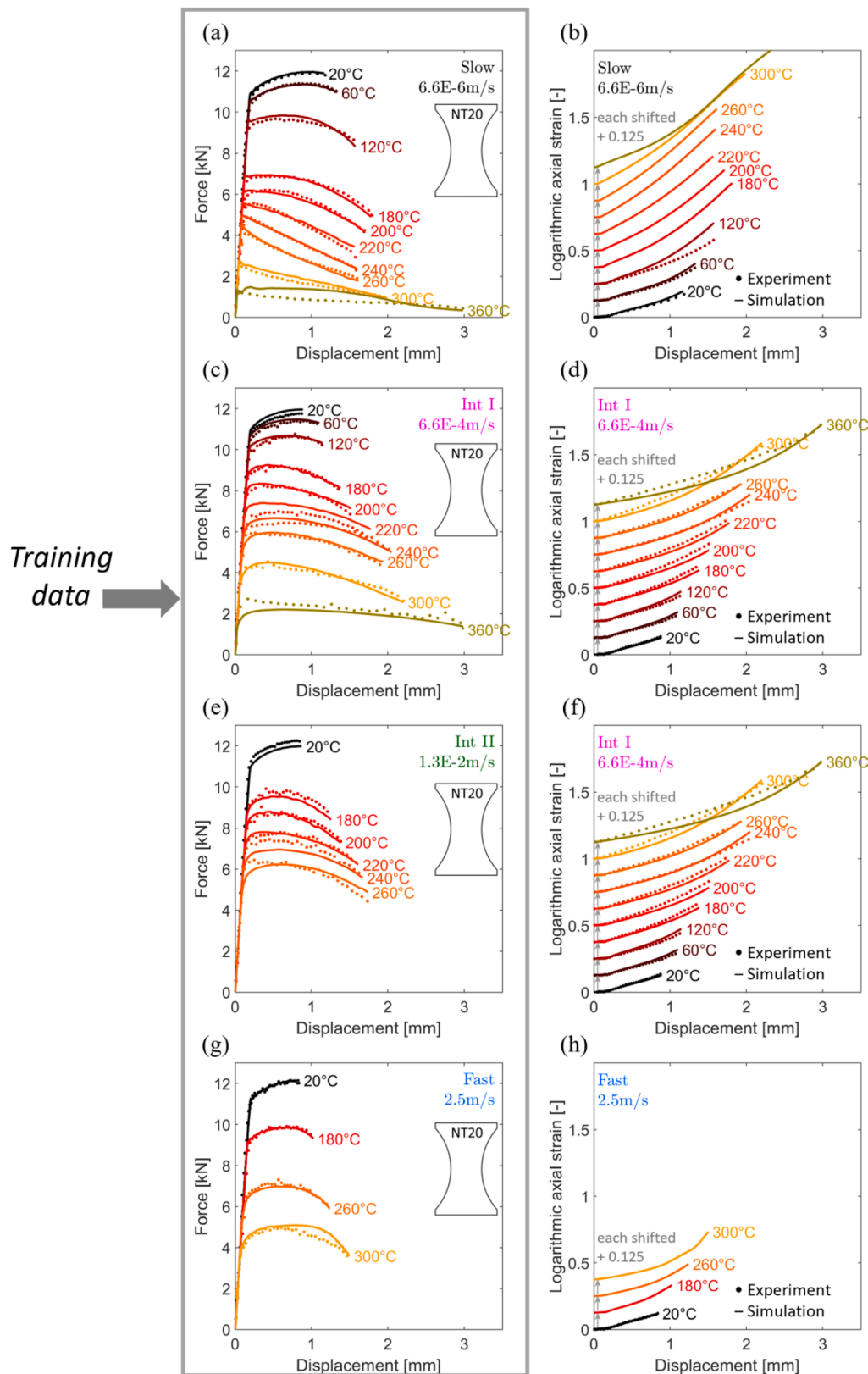


Fig. 9. Force–displacement curves of NT20 experiments obtained at displacement rates of (a) 6.6×10^{-6} m/s, (c) 6.6×10^{-4} m/s, (e) 1.3×10^{-2} m/s and (g) 2.5 m/s for various temperatures. Only NT20 force–displacement curves are used for training. The local strain measurements (b, d, f, h) are shifted up by 0.125 for readability. These local strain measurements serve as validation.

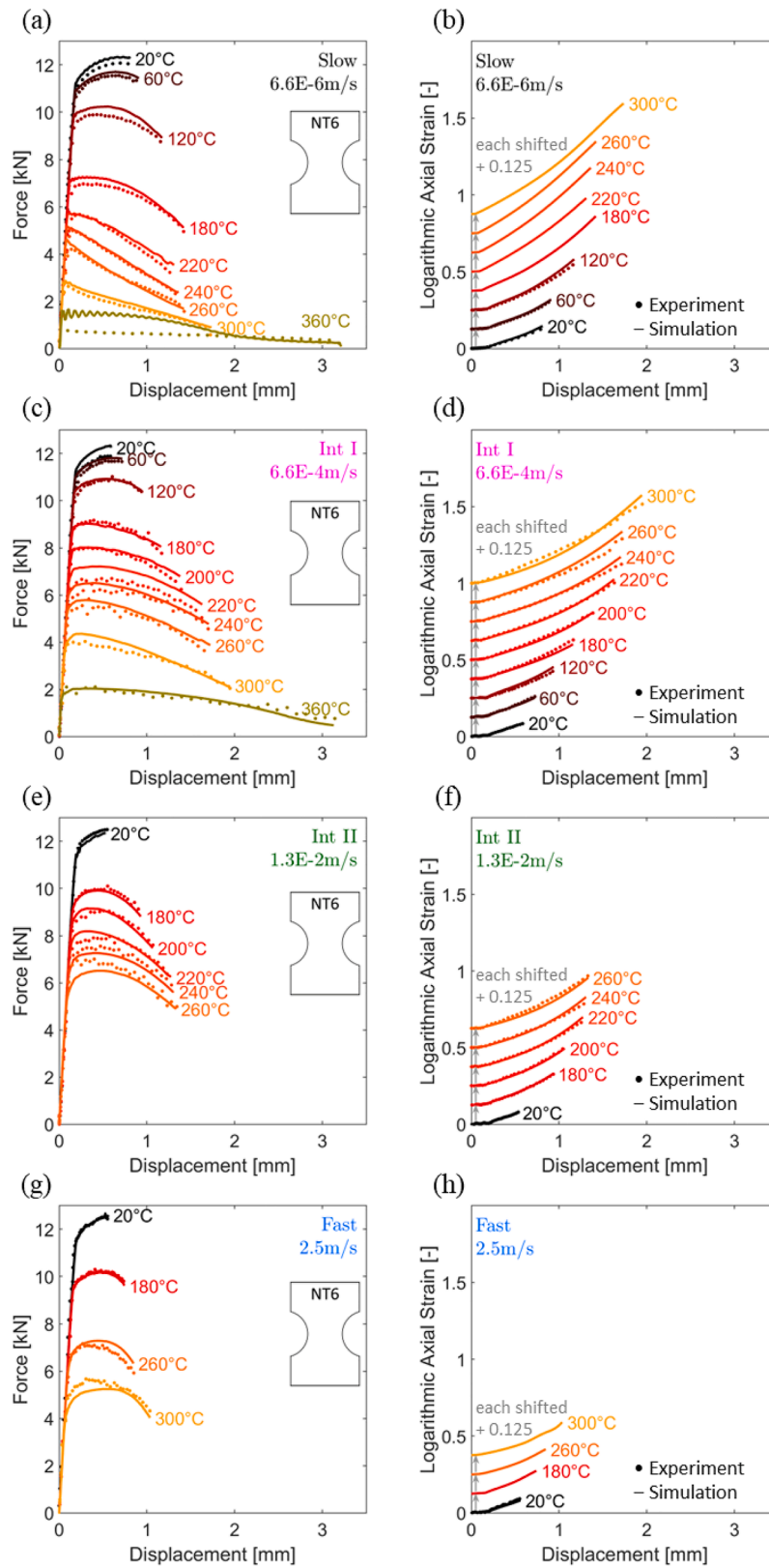


Fig. 10. Force–displacement curves of NT6 experiments obtained at displacement rates of (a) 6.6×10^{-6} m/s, (c) 6.6×10^{-4} m/s, (e) 1.3×10^{-2} m/s and (g) 2.5 m/s for various temperatures. The logarithmic axial strain from 1 mm local extensometers are plotted on the right column in (b) (d) (f) and (h). The NT6 experiments serve as validation.

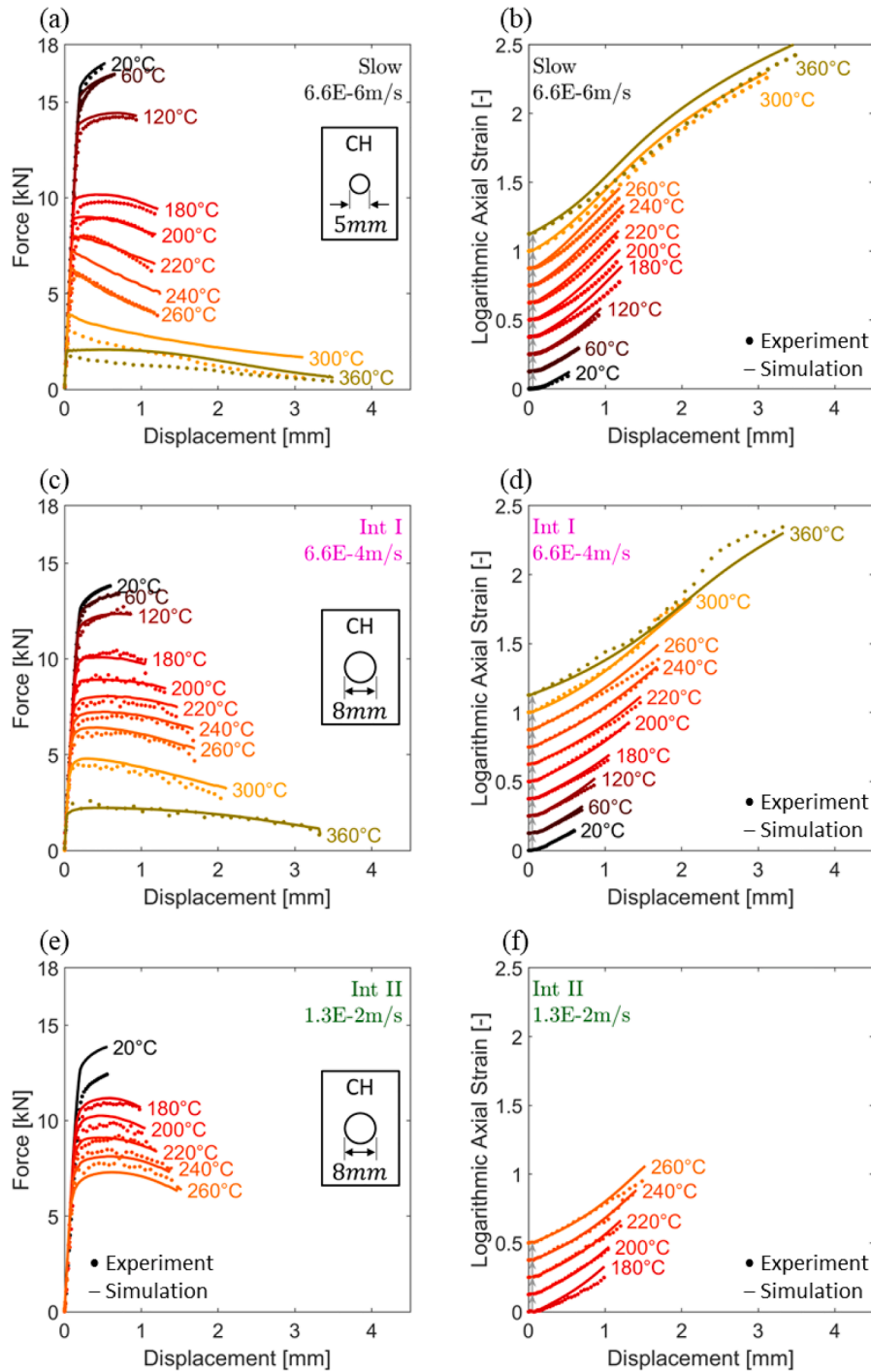


Fig. 11. Force–displacement curves of central hole (CH) experiments obtained at displacement rates of (a) 6.6×10^{-6} m/s, (c) 6.6×10^{-4} m/s, (e) 1.3×10^{-2} m/s for various temperatures. Note that for the slow speed a 5 mm diameter central hole is used, while for all other CH tests an 8 mm diameter was used due to limited clamping force. The local strain measurements (b, d, f) are shifted up by 0.125 for readability. The CH experiments serve as validation.

$$k[\bar{\epsilon}_p, \dot{\bar{\epsilon}}_p, T] = k_{SV}[\bar{\epsilon}_p] k_{NN}[\bar{\epsilon}_p, \dot{\bar{\epsilon}}_p, T]. \quad (13)$$

The reference strain hardening is a linear combination of Swift [76] and Voce [77] hardening laws with the weighting parameter $\alpha_{SV} \in [0, 1]$,

$$k_{SV}[\bar{\epsilon}_p] = \alpha_{SV} A (\epsilon_0 + \bar{\epsilon}_p)^n + (1 - \alpha_{SV}) \{k_0 + Q(1 - e^{-\beta \bar{\epsilon}_p})\}. \quad (14)$$

The formulation of the neural network $k_{NN}[\bar{\epsilon}_p, \dot{\bar{\epsilon}}_p, T]$ follows the format presented in Li et al. [64]. The network features three hidden layers of ten neurons, amounting to 297 model parameters (weights and biases). An overview of the NN based hardening model is shown in

Fig. 4.

3.2. Calibration of the plasticity model

The Yld2000-3D model parameters are identified following the procedures detailed in Gorji and Mohr [78]. The exponent $m = 8$ is chosen for FCC materials as recommended by Logan and Hosford [79]. The eight coefficients $\{\alpha_1, \alpha_2, \dots, \alpha_8\}$ are determined from the yield stress and Lankford ratios, which are extracted from uniaxial tension experiments along seven orientations (Table 1-2). The Swift $\{A, \epsilon_0, n\}$ and

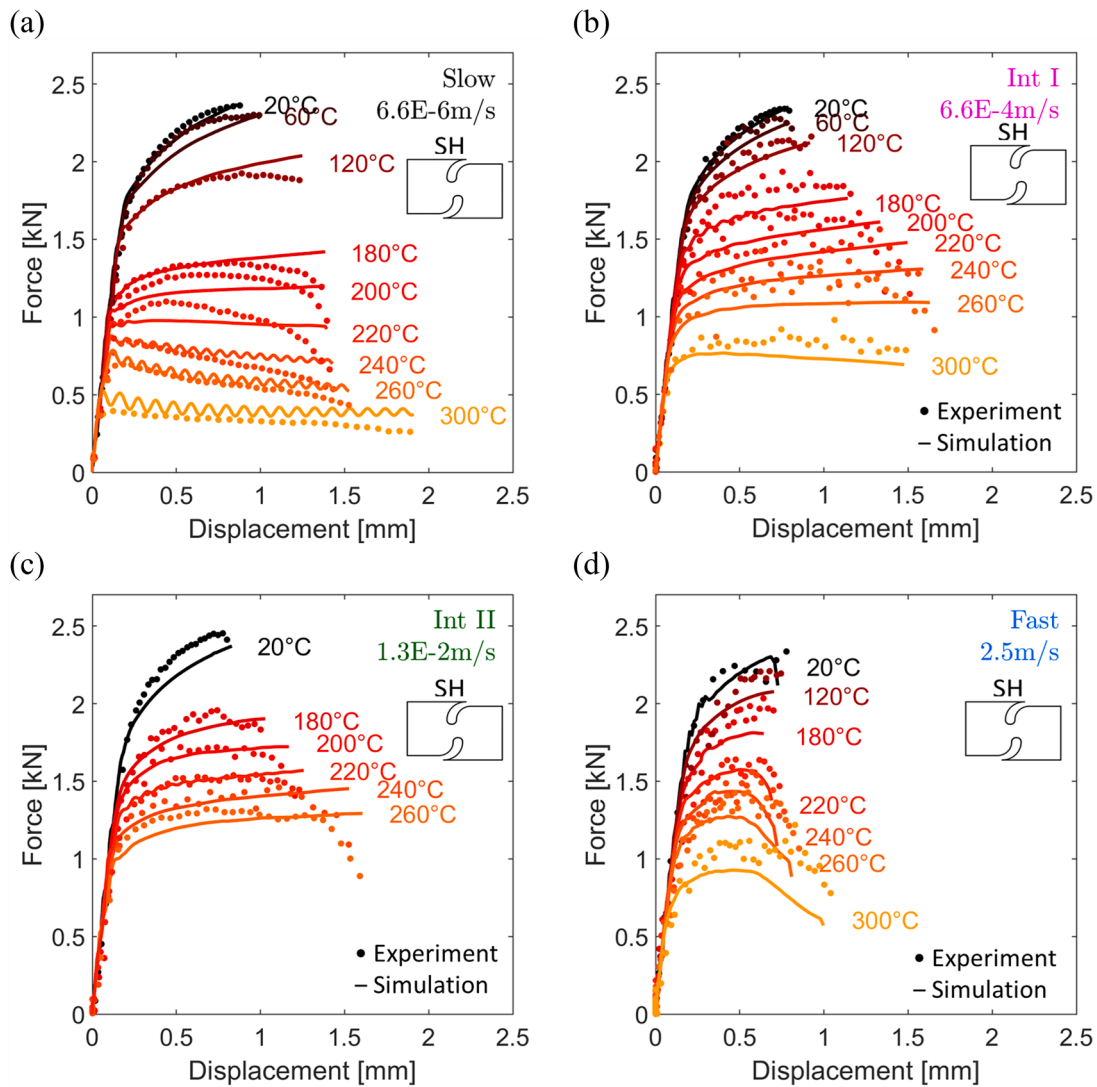


Fig. 12. Force–displacement curves of in-plane shear (SH) experiments obtained at displacement rates of (a) 6.6×10^{-6} m/s, (b) 6.6×10^{-4} m/s, (c) 1.3×10^{-2} m/s and (d) 2.5 m/s for various temperatures. The SH experiments serve as validation.

Voce $\{k_0, Q, \beta\}$ hardening parameters are determined from two independent least square fits of the true stress-plastic strain curves extracted from uniaxial tension test along the rolling direction. We obtain the weighting parameter α_{SV} from inverse fitting the quasi-static room temperature NT20 experiments [23].

The neural network based hardening function $k_{NN}[\bar{\epsilon}_p, \dot{\bar{\epsilon}}_p, T]$ is trained using the force displacement curves of NT20 experiments through a hybrid numerical-experimental approach. This requires repeatedly running FE simulations to minimize the difference between the simulated and the experimental force-displacement curves. Coupled thermal-mechanical simulations are performed with Abaqus/explicit using first-order solid elements (C3D8RT). A constant Taylor-Quinney coefficient of 0.9 is chosen. High-speed infrared imaging shows that the temperature at the boundary of the gauge section remains constant throughout the test. Hence, a constant temperature boundary condition is applied along the boundaries of the simulated gauge section. The rest of the sample surfaces are treated as adiabatic. An element edge length of 0.125 mm is chosen in the gage section, corresponding to 16 elements through the thickness (or 8 elements through half thickness). One-eighth of the notched tension and central-hole specimens are simulated due to symmetry, while the shear specimen is simulated with full thickness (Fig. A 1). We employ mass-scaling with more than 10^5 time steps to accelerate low strain rate simulations.

Together with the Yld2000-3D plasticity framework, the neural network hardening law is implemented into a user-material subroutine (VUMAT). During the training process, a counter-example regularization technique is employed to enforce positive strain rate sensitivity [65], thereby guaranteeing the convergence of the elastoplastic return-mapping algorithm.

4. Fracture modeling

We present the novel extension of the Hosford–Coulomb (HC) fracture model into the strain rate and temperature domain. The section starts by introducing the damage accumulation framework to account for non-proportional loading, followed by the formulation of the neural network-based HC model. The calibration procedure for this NN based HC model with loading paths featuring evolving (non-constant) stress triaxiality η , Lode angle parameter $\bar{\theta}$, equivalent plastic strain $\bar{\epsilon}_p$, strain rate $\dot{\bar{\epsilon}}_p$ and temperature T is provided.

4.1. Damage indicator model

A damage indicator model is proposed to predict the onset of fracture for a given loading path to fracture. This involves introducing a damage indicator variable D that, starting from zero for the undeformed

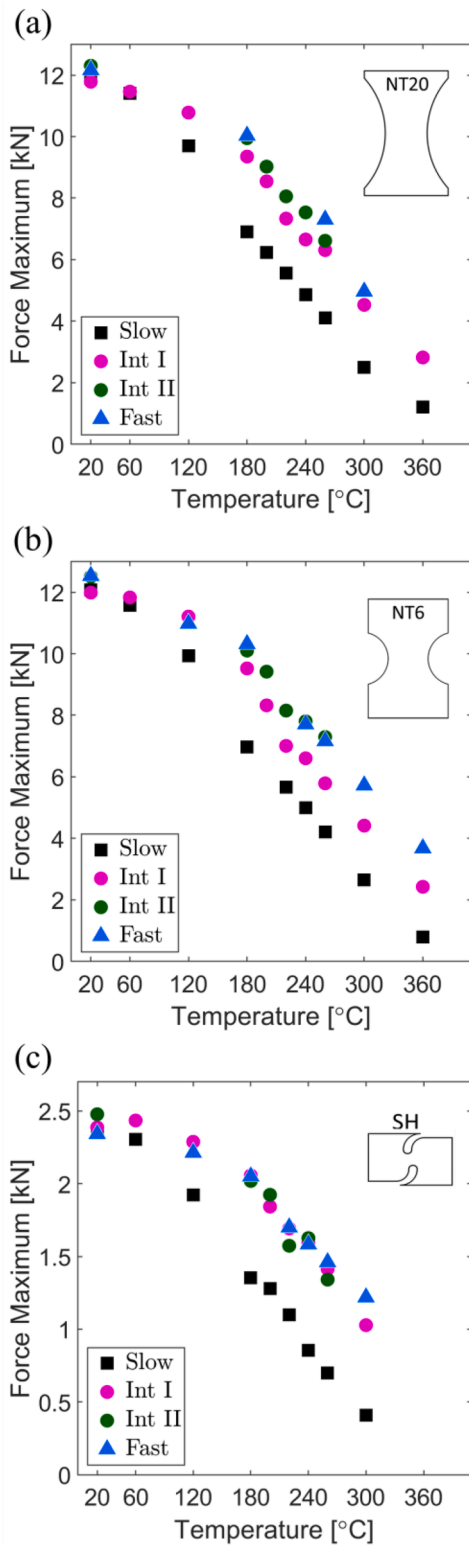


Fig. 13. The extracted force-maximum as a function of initial temperature at four loading speeds from (a) NT20, (b) NT6 and (c) SH experiments.

material, increases monotonically as the material deforms plastically,

$$dD = \frac{d\bar{\epsilon}_p}{\bar{\epsilon}_f^{pr}[\eta, \bar{\theta}, \dot{\bar{\epsilon}}_p, T]} \quad (15)$$

The effects of stress state, strain rate and temperature are introduced through the function $\bar{\epsilon}_f^{pr}[\eta, \bar{\theta}, \dot{\bar{\epsilon}}_p, T]$ which corresponds to the equivalent

Table 3

Normalization ranges of the NN based hardening function. Note that the output layers feature the hyperbolic tangent activation function.

	Variable	Unit	Min	Max
Input	$\bar{\epsilon}_p$	[-]	0.001	3
	$\log(\dot{\bar{\epsilon}}_p)$	[s ⁻¹]	-9	12
Output	T	[°C]	0	500
	k_{NN}	[-]	0.1	2

plastic strain at the onset of fracture under proportional isothermal loading at constant strain rate. Fracture is then assumed to initiate when $D = 1$. In other words, we have an integral condition,

$$D = \int_0^{\bar{\epsilon}_f} \frac{d\bar{\epsilon}_p}{\bar{\epsilon}_f^{pr}[\eta, \bar{\theta}, \dot{\bar{\epsilon}}_p, T]} = 1 \quad (16)$$

that determines the fracture strain $\bar{\epsilon}_f$ for a given loading history. Within the damage indicator framework, the fracture model response is defined by the specific form of the function $\bar{\epsilon}_f^{pr}[\eta, \bar{\theta}, \dot{\bar{\epsilon}}_p, T]$.

4.2. Neural network based Hosford–Coulomb model

A highly versatile and flexible fracture model is obtained when representing the entire function $\bar{\epsilon}_f^{pr}[\eta, \bar{\theta}, \dot{\bar{\epsilon}}_p, T]$ through a neural network [66],

$$\bar{\epsilon}_f^{pr} = f_{NN}[\eta, \bar{\theta}, \dot{\bar{\epsilon}}_p, T]. \quad (17)$$

The shortcoming of this approach is that it requires very large amounts of training data in the 5D space of stress triaxiality η , Lode angle parameter $\bar{\theta}$, equivalent plastic strain $\bar{\epsilon}_p$, strain rate $\dot{\bar{\epsilon}}_p$ and temperature T due to its flexibility. Pandya et al. [66] achieved this through the artificial augmentation of their training data sets.

Here, a new approach is proposed. Firstly, we constrain the fracture model such that the stress state dependence (for a given strain rate and temperature) is governed by the Hosford–Coulomb (HC) fracture initiation model ([23]). For proportional loading histories, the latter reads

$$\bar{\epsilon}_f^{HC}[\eta, \bar{\theta}, a, b, c] = b(1 + c)^{\frac{1}{n}} \left(\left\{ \frac{1}{2} ((f_1 - f_2)^a + (f_2 - f_3)^a + (f_1 - f_3)^a) \right\}^{\frac{1}{a}} + c(2\eta + f_1 + f_3) \right)^{-\frac{1}{n}} \quad (18)$$

with the model parameters a , b , and c , the fixed transformation parameter $n = 0.1$, and the Lode angle dependent trigonometric functions,

$$\begin{aligned} f_1[\bar{\theta}] &= \frac{2}{3} \cos \left[\frac{\pi}{6} (1 - \bar{\theta}) \right], \\ f_2[\bar{\theta}] &= \frac{2}{3} \cos \left[\frac{\pi}{6} (3 + \bar{\theta}) \right], \\ f_3[\bar{\theta}] &= -\frac{2}{3} \cos \left[\frac{\pi}{6} (1 + \bar{\theta}) \right]. \end{aligned} \quad (19)$$

The HC model effectively defines a surface that describes the fracture strain $\bar{\epsilon}_f^{HC}$ as a function of the stress triaxiality η and the Lode angle parameter $\bar{\theta}$ (Fig. 5a). The parameter b controls the overall magnitude of the fracture strain, the parameter a affects the Lode angle dependency, while the parameter c controls both the effects of the Lode angle and the stress triaxiality. For plane stress conditions, the Lode angle parameter may be expressed as a function of the stress triaxiality (solid line). This allows the HC model to be visualized in the $[\eta, \bar{\epsilon}_f^{HC}]$ plane (Fig. 5b) or the $[\bar{\theta}, \bar{\epsilon}_f^{HC}]$ plane (Fig. 5c).

Secondly, we render the Hosford–Coulomb model strain rate and temperature dependent by expressing its defining parameters $[a, b, c]$ as

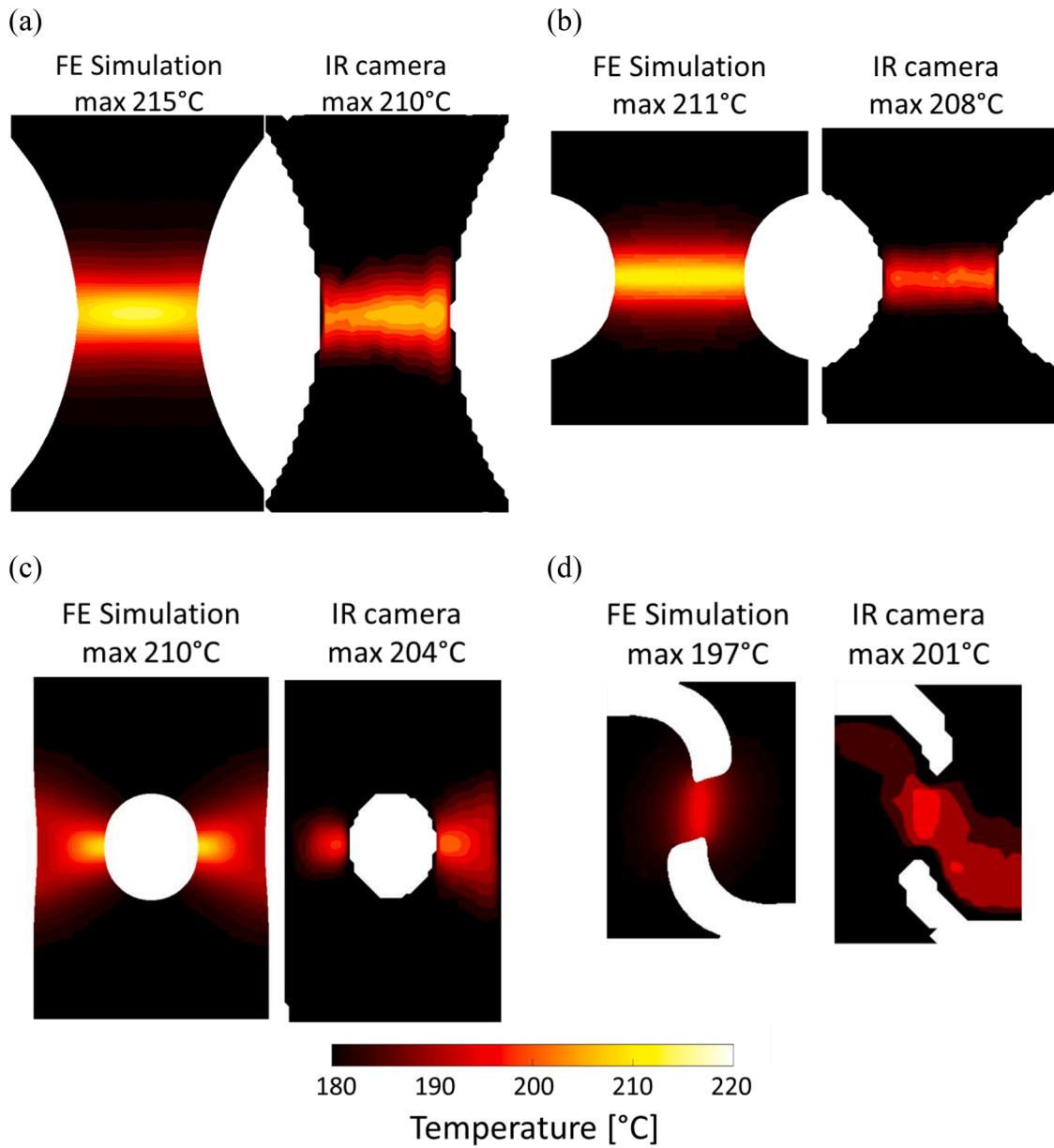


Fig. 14. FE-predicted surface temperature compared to IR measured surface temperature of (a) NT20, (b) NT6, (c) CH, and (d) SH specimens. All experiments are performed at an initial temperature of 180 °C and loading speed of 1.3×10^{-2} m/s (Int II). Up to 64 pixels are available along the sample width direction due to the limited resolution.

a neural network function of the strain rate and temperature, i.e.

$$\mathbf{f}_{NN}[\dot{\bar{\epsilon}}_p, T] = \begin{pmatrix} a \\ b \\ c \end{pmatrix}. \quad (20)$$

The neural-network based rate- and temperature-dependent Hosford–Coulomb model then reads

$$\bar{\epsilon}_f^{pr}[\eta, \bar{\theta}, \dot{\bar{\epsilon}}_p, T] = \bar{\epsilon}^{HC}[\eta, \bar{\theta}, \mathbf{f}_{NN}[\dot{\bar{\epsilon}}_p, T]]. \quad (21)$$

4.3. Gradient calculation

We choose a mean squared error loss function to guide the identification of the weights W_{kl} that specify the neural network function \mathbf{f}_{NN} . For each experiment $j \in [1, \dots, n_{exp}]$, we compute the damage indicator D_j up to the point of fracture initiation through numerical integration. The result is then compared with the ground truth ($D = 1$) to quantify the

error,

$$Loss = \frac{1}{2n_{exp}} \sum_j^{n_{exp}} (D_j - 1)^2 \quad (22)$$

Neural networks are typically trained using a gradient descent minimization framework (e.g. [80,81]). For each weight parameter W_{kl} of the neural network, the learning rule requires the computation of the gradient $\partial Loss / \partial W_{kl}$ to update the weights,

$$\Delta W_{kl} = -\eta_l \frac{\partial Loss}{\partial W_{kl}}. \quad (23)$$

Fig. 6 includes a schematic that outlines the training procedure. The process of calculating the partial derivative $\partial Loss / \partial W_{kl}$ is broken down into four steps:

Step 1. We have

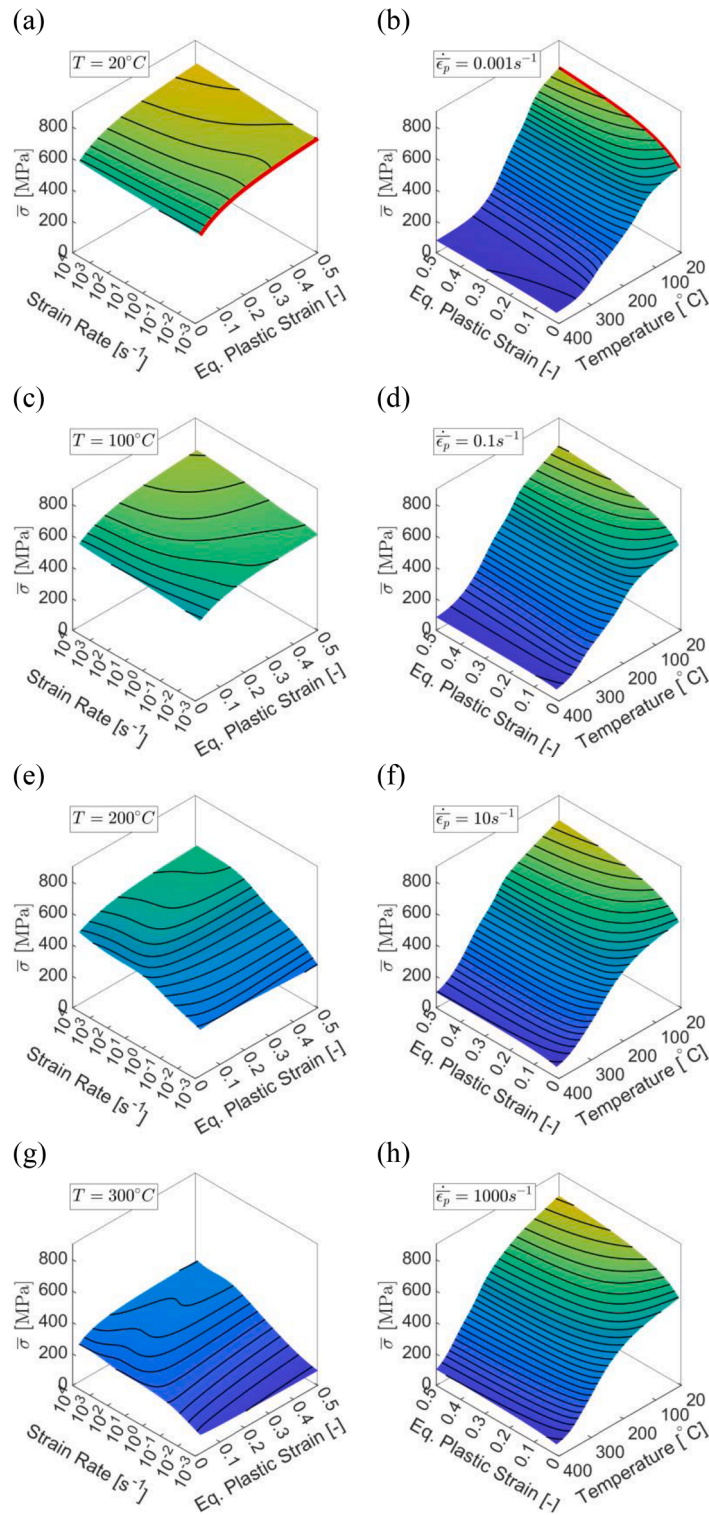


Fig. 15. 3D visualization of the NN based hardening model for fixed temperatures of 20° to 300 °C, and fixed strain rates of 0.001/s to 1000/s. The red curve in (a) and (b) highlight the room temperature quasi-static (0.001/s) response of the material.

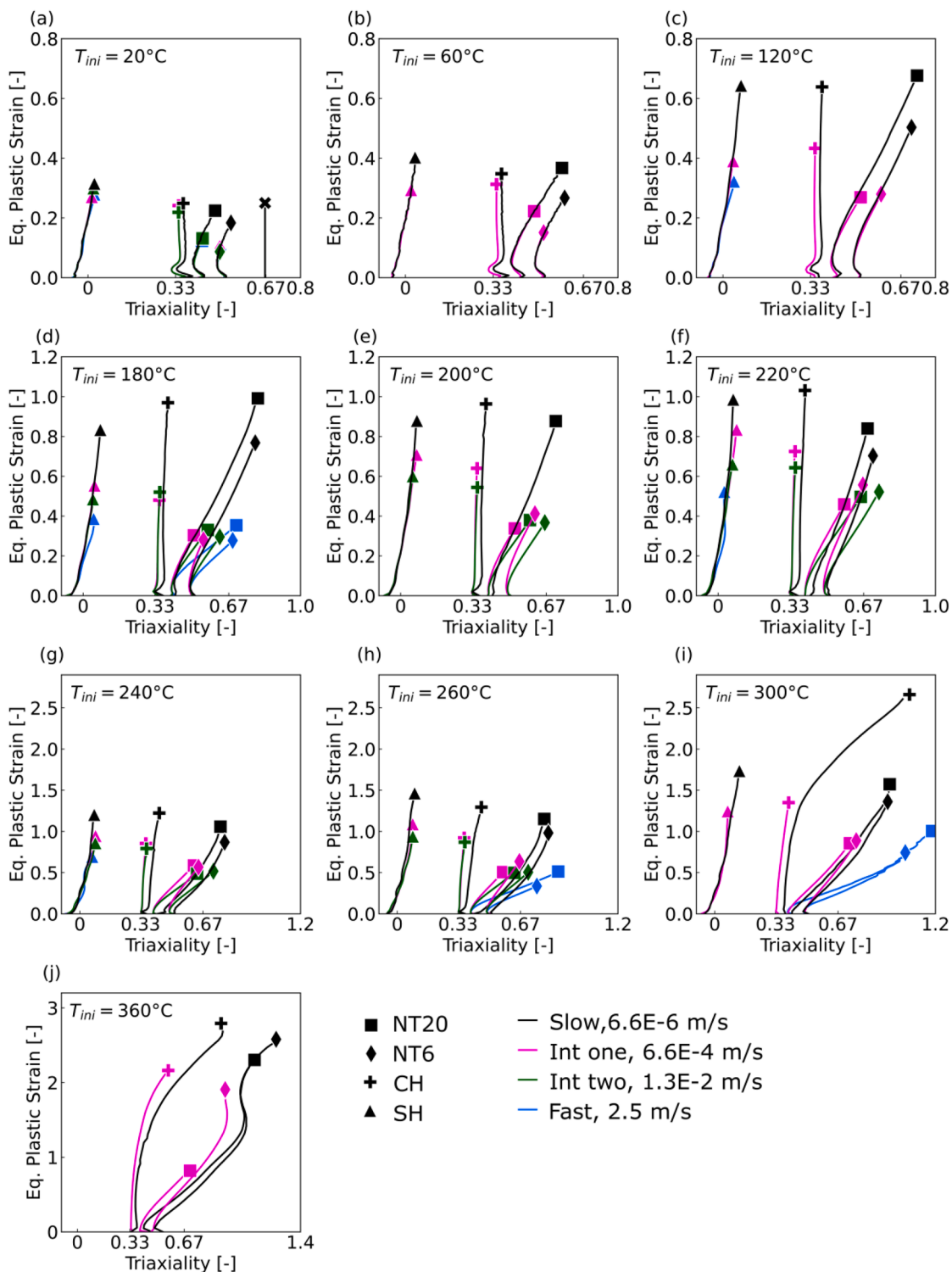


Fig. 16. Evolution of equivalent plastic strain as a function of stress triaxiality for different initial temperatures. SH, CH, NT20 and NT6 specimens are highlighted with triangle, cross, square and diamond, respectively. The loading speeds are colored by 6.6×10^{-6} m/s (black), 6.6×10^{-4} m/s (magenta), 1.3×10^{-2} m/s (green), and 2.5 m/s (blue). All loading paths are non-proportional, featuring an evolution in stress triaxiality and Lode angle parameter.

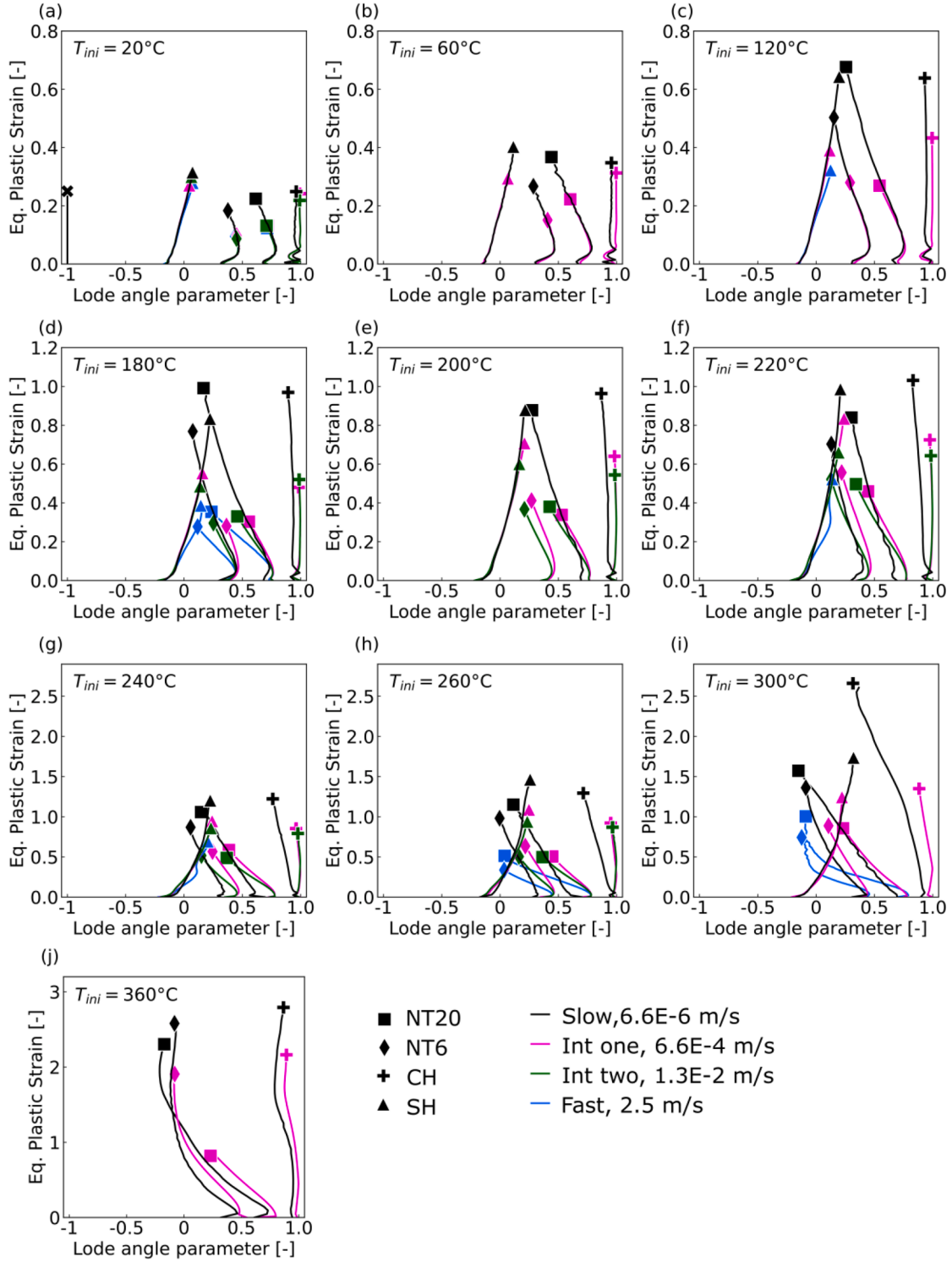


Fig. 17. Evolution of equivalent plastic strain as a function of the Lode angle parameter for different initial temperatures. Note the evolving triaxiality and Lode angle parameter for all paths.

$$\frac{\partial Loss}{\partial W_{kl}} = \sum_j^{n_{exp}} \frac{\partial Loss}{\partial D_j} \frac{\partial D_j}{\partial W_{kl}}, \quad (24)$$

$$\frac{\partial Loss}{\partial D_j} = \frac{1}{n_{exp}} (D_j - 1). \quad (25)$$

where the term $\frac{\partial Loss}{\partial D_j}$ is obtained directly from the quadratic cost function (Eq. 22),

Step 2. Subsequently, we decompose the term $\frac{\partial D_j}{\partial W_{kl}}$ for each experiment number j . Discretizing the loading path, the damage may be written as the sum of n_{INC} increments,

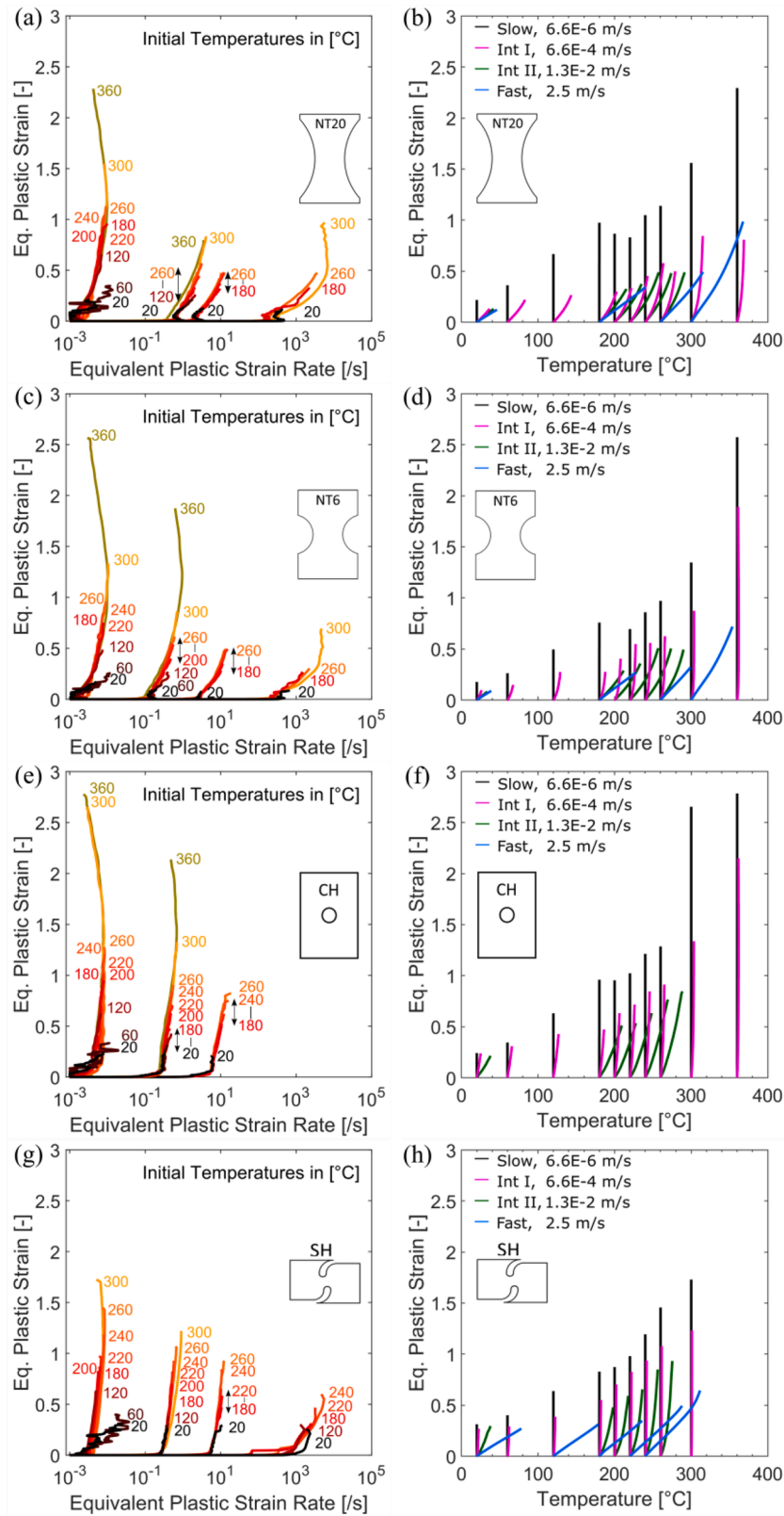


Fig. 18. Evolution of equivalent plastic strain as a function of strain rate for (a) NT20, (c) NT6, (e) CH and (g) SH tests. The evolution of equivalent plastic strain and temperature of all experiments is shown in (b), (d), (f) and (h). Note the rise in temperature during tests at elevated strain rates.

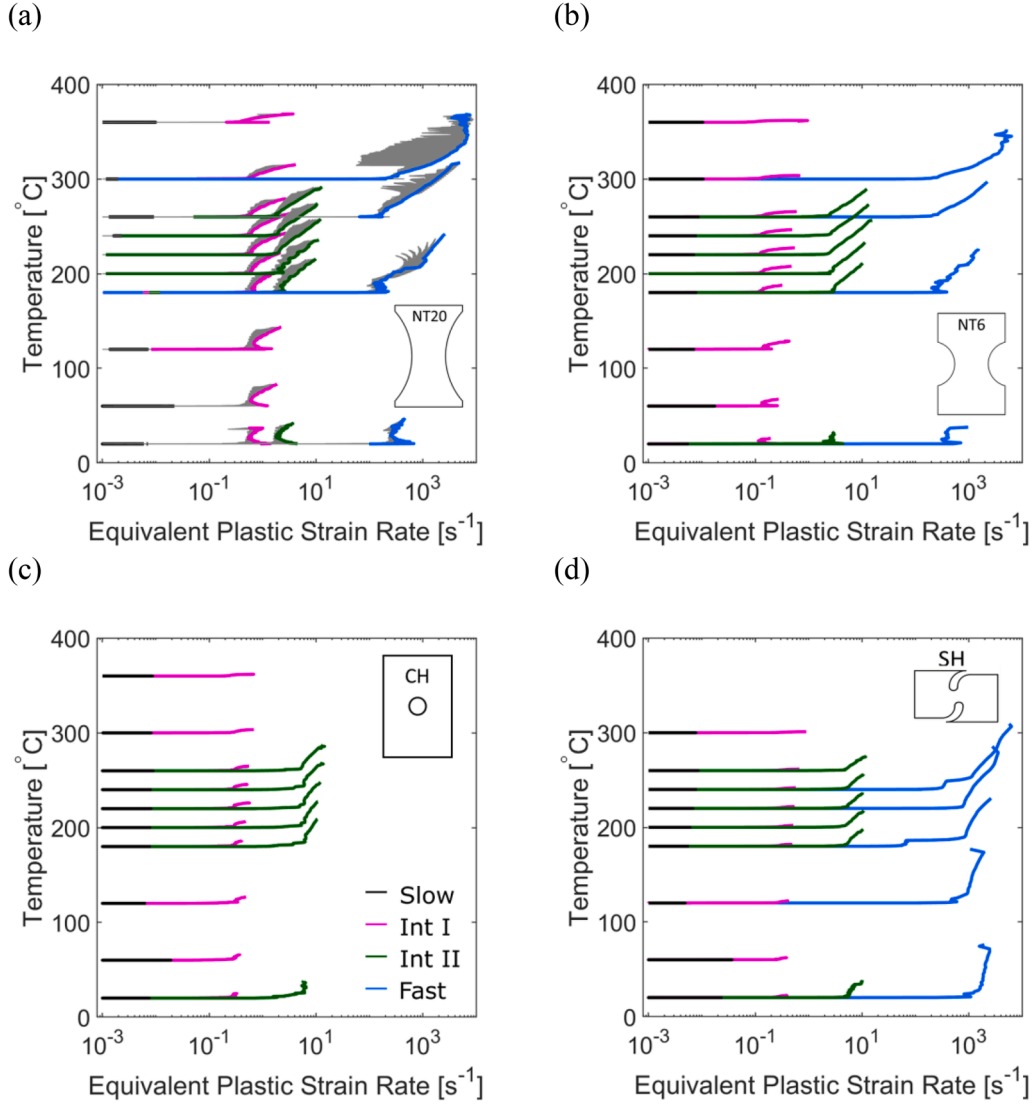


Fig. 19. Evolution of the temperature as a function of strain rate for (a) NT20, (b) NT6, (c) CH and (d) SH tests from the element with the highest equivalent plastic strain. The gray curves in (a) denote the strain rate and temperature histories extracted from all elements on the mid-plane of the NT20 specimen. Note the rise in strain rate due to localized necking and the rise in temperature due to plastic dissipation.

$$D_j = \sum_i^{n_{INC}} \frac{\Delta \bar{\epsilon}_i^p}{\bar{\epsilon}_i^{HC}} \quad \text{with} \quad (26)$$

$$\bar{\epsilon}_i^{HC} = \bar{\epsilon}^{HC} \left[\eta_i, \bar{\theta}_i, \mathbf{f}_i^{NN} \left[\bar{\epsilon}_p^{(i)}, T_i \right] \right].$$

Applying the chain rule into the summation for experiment j and increment i , we have

$$\frac{\partial D_j}{\partial W_{kl}} = \sum_i^{n_{INC}} \left(- \frac{\Delta \bar{\epsilon}_i^p}{(\bar{\epsilon}_i^{HC})^2} \frac{\partial \bar{\epsilon}_i^{HC}}{\partial \mathbf{f}_i^{NN}} \frac{\partial \mathbf{f}_i^{NN}}{\partial W_{kl}} \right). \quad (27)$$

Combining Steps 1 and 2 yields:

$$\frac{\partial Loss}{\partial W_{kl}} = \frac{1}{n_{exp}} \sum_j^{n_{exp}} (1 - D_j) \sum_i^{n_{INC}} \left(\frac{\Delta \bar{\epsilon}_i^p}{(\bar{\epsilon}_i^{HC})^2} \frac{\partial \bar{\epsilon}_i^{HC}}{\partial \mathbf{f}_i^{NN}} \frac{\partial \mathbf{f}_i^{NN}}{\partial W_{kl}} \right) \quad (28)$$

Step 3. The third step evaluates the partial derivative of the HC fracture strain $\bar{\epsilon}_i^{HC}$ with respect to the network output \mathbf{f}_i^{NN} . This is achieved through a numerical derivative of the HC model with respect to its parameters at the current stress state $(\eta_i, \bar{\theta}_i)$,

$$\frac{\partial \bar{\epsilon}_i^{HC}}{\partial \mathbf{f}_i^{NN}} = \left[\frac{\partial \bar{\epsilon}_i^{HC}}{\partial a_i}, \frac{\partial \bar{\epsilon}_i^{HC}}{\partial b_i}, \frac{\partial \bar{\epsilon}_i^{HC}}{\partial c_i} \right]^T. \quad (29)$$

Step 4. The remaining term $\frac{\partial \mathbf{f}_i^{NN}}{\partial W_{kl}}$ is the derivative of the neural network function with respect to the weights, which is conveniently obtained through standard back-propagation

$$\frac{\partial \mathbf{f}_i^{NN}}{\partial W_{kl}} = \left[\frac{\partial a_i}{\partial W_{kl}}, \frac{\partial b_i}{\partial W_{kl}}, \frac{\partial c_i}{\partial W_{kl}} \right]^T. \quad (30)$$

4.4. Choice of the optimizer and network size (hyperparameters)

The optimization framework for the fracture modeling neural network is constructed in Python 3.9.11. We obtain the partial derivative $\partial \mathbf{f}_i^{NN} / \partial W_{kl}$ using the gradient tape function in TensorFlow 2.6.0. Following the formulation of Riedmiller and Braun [82], we coded the resilient-back propagation (RPROP) optimizer in the TensorFlow framework. Comparable accuracies are achieved using the Adam

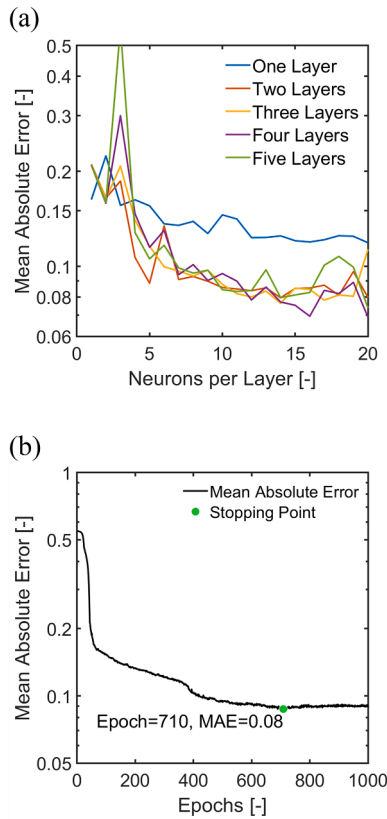


Fig. 20. (a) NN-parameterized fracture model: effective mean absolute error on terminal damage after training for maximum 1000 epochs for various network width and depth combinations, using the RPROP optimizer. A two layer network with ten neuron each layer is chosen, as a compromise between performance and network size. (b) Early stopping is activated at epoch 710 to prevent over-fitting, where the mean absolute error reaches a minimum and stops decreasing.

Table 4

Normalization ranges of the NN parameterized fracture model. Note that the output layers feature the hyperbolic tangent activation function.

	Variable	Unit	Min	Max
Input	$\log(\dot{\bar{\epsilon}}_p)$	$[s^{-1}]$	-9	10
	T	$[^{\circ}C]$	0	500
Output	a	$[-]$	1.0	2.0
	b	$[-]$	0.2	3.0
	c	$[-]$	0	0.12

optimizer (Fig. A 2) by Kingma and Ba [83], with greater performance variations for networks with many layers. During training, we also introduce a clipping function to prevent overfitting. The clipped loss reads

$$Loss = \frac{1}{2n_{exp}} \sum_j^{n_{exp}} (\text{Clip}[D_j - 1])^2 \quad (31)$$

with

$$\text{Clip}[x] = \begin{cases} x, & |x| > 0.05 \\ 0, & |x| \leq 0.05 \end{cases} \quad (32)$$

The goal here is to penalize samples with large error on the damage D_j , while redirecting the optimization focus from the samples whose terminal damage D_j lies within the range $D_j \in [0.95, 1.05]$.

5. Results and discussion

The experimental results are first summarized in this section, indicating an increase in strain rate sensitivity at higher temperature for aluminum AA7075-T6. Predictions of the plasticity model are compared with experimental measurements, showcasing good agreement at large-deformation. The loading paths to fracture are used to calibrate the neural network based Hosford–Coulomb fracture model, which is visualized in the stress state domain $[\eta, \bar{\theta}]$ and the rate- and temperature domain $[\dot{\bar{\epsilon}}_p, T]$.

5.1. Experimental results

5.1.1. Uniaxial tension at room temperature

Uniaxial tension experiments are performed at room temperature for seven different angles (0° , 15° , 30° , 45° , 60° , 75° and 90°) between the tensile direction and the rolling direction (Table 1). A summary of the engineering stress-strain curves is presented in Fig. 7a. The material shows low strain hardening irrespective of the material orientation, with less than 100 MPa increase from the yield stress to the ultimate tensile strength (UTS). The highest UTS (561 MPa) is measured in the rolling direction (0°), while the lowest tensile strength (542 MPa) is observed for the 60° orientation. The corresponding yield stress ratios (black dots) and Lankford values (blue dots) are plotted in Fig. 7b. Overall, the material shows a mild anisotropy in the yield stress ratios, ranging from 0.96 (45°) to 1.01 (90°), while the r-values ranging from 0.59 (0°) to 1.09 (45°).

5.1.2. Experiments at elevated strain rates and temperatures

Fig. 8a-d summarize the experimentally-measured engineering stress-strain curves from uniaxial tension (UT) experiments at various strain rates and temperatures. Out of the two repeats, only one representative curve is shown for readability. We truncate the curves once a crack is visible on the specimen surface. At temperatures below $60^{\circ}C$, the material shows almost no strain rate hardening for low and intermediate strain rates ($<2/s$) - only at a strain rate of 110/s, an increase in yield strength of 4.4% (22 MPa) is observed (Fig. 8e–f). However, when further increasing the temperature ($>120^{\circ}C$), the viscous effect begins to play a much more significant role. For example, increasing the strain rate from 0.001/s to 0.1/s leads to a 21% increase in yield stress at $180^{\circ}C$ (Fig. 8f), while the same strain rate difference would cause a 90% rise in yield stress at $360^{\circ}C$. It is noteworthy that at a strain rate of 0.001/s and high temperatures (above $240^{\circ}C$) necking occurs at very low strains, making a direct experimental measurement of the large deformation response impossible. Across all UT tests, an increase in temperature results in a reduction of the yield strength and the strain hardening rate. For example, when increasing the temperature from $20^{\circ}C$ to $360^{\circ}C$ the yield stress reduces by a factor of 9.5. An overview of the 0.2% offset yield stress for all UT experiments is given in Fig. 8e.

Across all combinations of stress states, strain rates and temperatures, i.e. NT20 (Fig. 9), NT6 (Fig. 10), CH (Fig. 11) and SH (Fig. 12) similar trends are observed in the measured force–displacement curves (dotted curves) as for their UT counterparts. The material shows a low strain rate sensitivity at room temperature and a higher strain rate sensitivity at elevated temperatures. For example, the room temperature NT20 tests stay within 3% (0.5 kN) range of each other. In contrast, a 45% increase in maximum force is observed at $180^{\circ}C$ when increasing from low to fast loading speeds (Fig. 9 and Fig. 13).

Apart from higher reaction forces, experiments at higher loading speeds also exhibit a lower displacement to fracture. At $180^{\circ}C$, NT20 experiments fracture at a displacement of 1.79 mm at 6.6×10^{-6} m/s, 1.35 mm at 6.6×10^{-4} m/s, 1.21 mm at 1.3×10^{-2} m/s, and 0.99 mm at 2.5 m/s. For all specimen types, we observe higher fracture displacements with increasing temperature. For example, the NT6 low speed tests feature a fracture displacement of 3.4 mm at $360^{\circ}C$, approximately

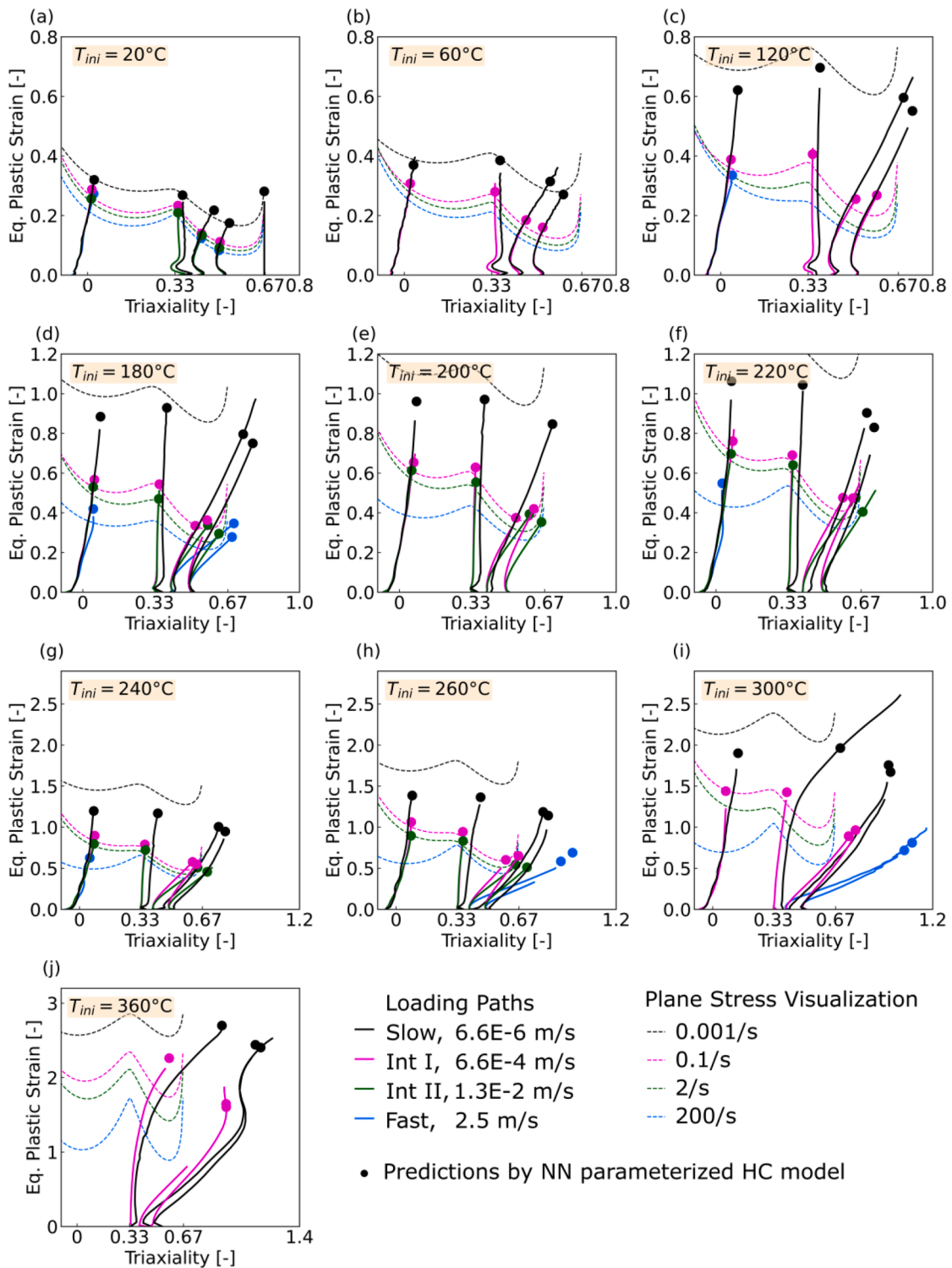


Fig. 21. NN parameterized Hosford-Coulomb fracture onset (solid dots) calculated using full loading paths (solid lines). The NN predicted fracture loci for plane stress conditions are highlighted in dashed lines.

four times higher than the fracture displacement at 20°C (0.83 mm). In addition, the higher fracture displacements also correspond to higher local axial strain measurements, which are taken from 1 mm long virtual extensometers on the specimen surface (red dots in Fig. 2). Comparing the CH specimens at 6.6×10^{-4} m/s (Fig. 11c-d), the axial strain at fracture increases more than eight times from 20°C (0.15) to 360°C (1.22). Note that the axial strain measurements are each shifted up by 0.125 for better visibility.

Fig. 13 summarized the force maxima observed in the NT20, NT6 and SH experiments. The plots elucidate the monotonic effect of the temperature, i.e. the higher the temperature, the softer the specimen response. Furthermore, they show the positive strain rate effect on the force maximum which becomes more pronounced for higher temperatures.

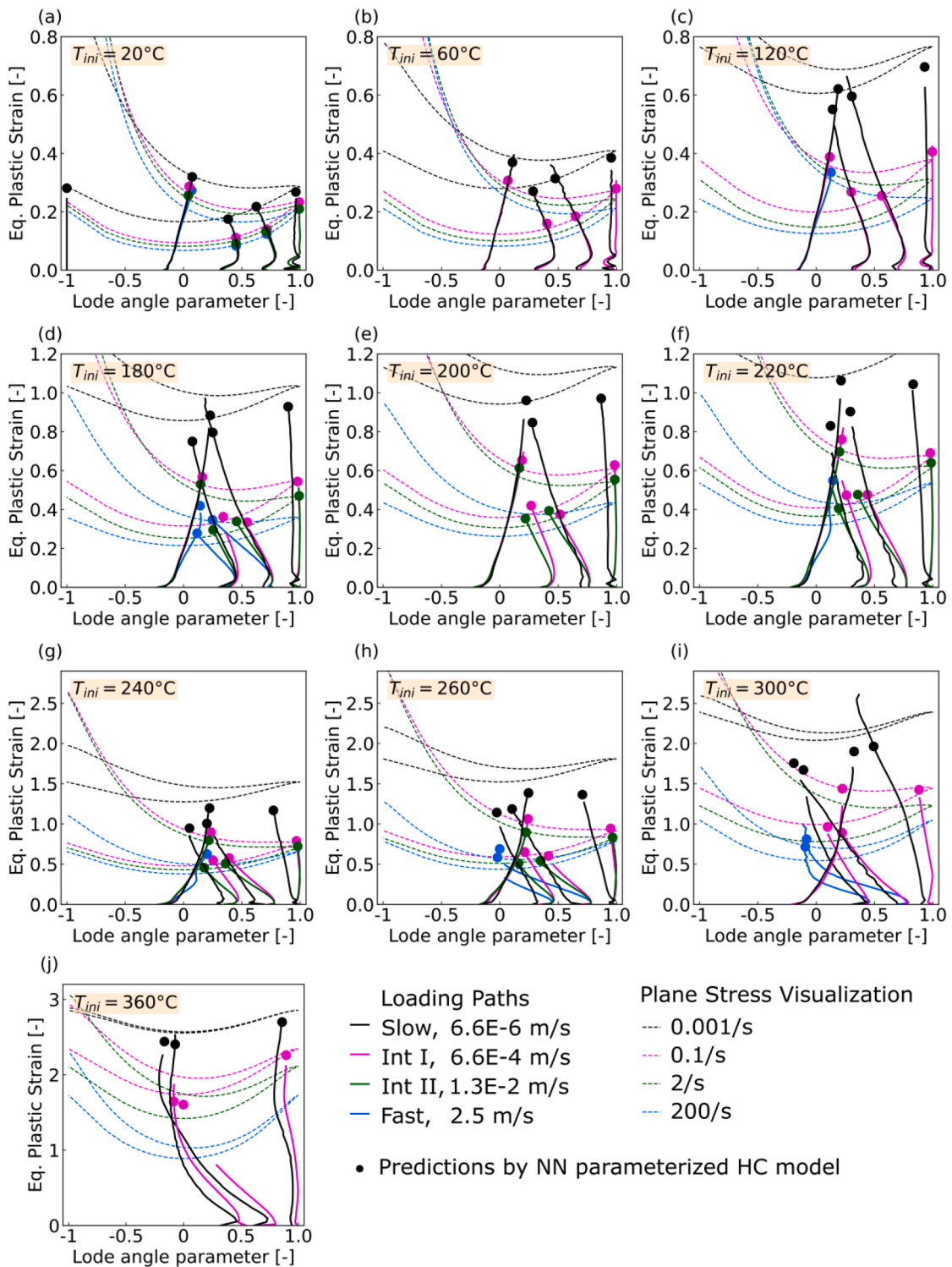


Fig. 22. NN parameterized Hosford-Coulomb fracture onset (solid dots) calculated using full loading paths (solid lines). The NN predicted fracture loci for plane stress conditions are highlighted in dashed lines.

5.2. Plasticity model training and validation

Fig. 7c depicts the identified Yld2000 yield locus for plane stress conditions. The model parameters are calibrated so that the r -value and yield stress values for uniaxial tension are captured accurately (compare the solid lines with the experimental results in Fig. 7b). In addition, a finite element simulation of the shear experiment is used to identify the biaxial yield stress ratio (black solid line, Fig. 12a).

The hardening law is identified based on the results from the NT20 specimens with a mean squared error of 0.039 kN² after 500 epochs. This result was obtained after 620 h of training on a high performance computing cluster (using 100 cores). Fig. 9 shows the predictions of the trained model (solid lines) next to the force-displacement curves included in the training dataset (solid dots).

Overall, the rate- and temperature dependent response of the material is captured with good accuracy. The highest calibration error is

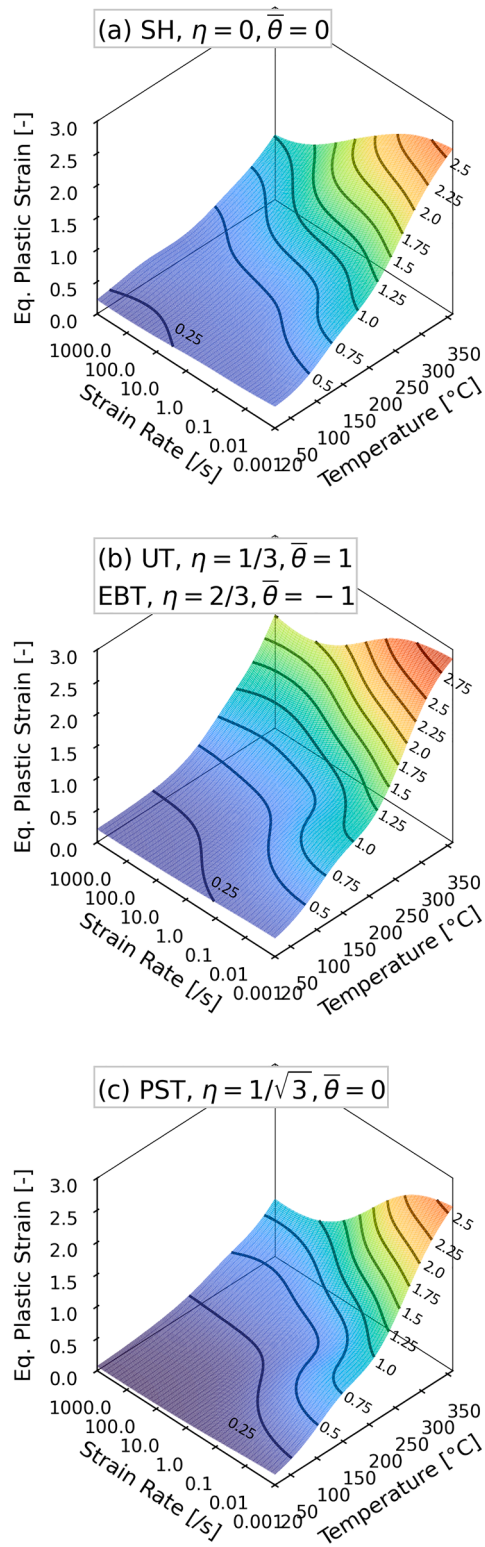


Fig. 23. Fracture strain under proportional loading for stress states of uniaxial tension (UT), shear (SH), plane strain tension (PST) and equi-biaxial tension (EBT). The equivalent plastic strain at fracture is visualized as a function of strain rate and temperature.

observed for the highest temperatures, e.g. the low speed 360 °C case FE simulation over-estimates the experimental force measurement by 0.48 kN (60%). The maximum difference on the local strain measurements (0.06) is also obtained for 360 °C. According to the UT yield stress

measurements (Fig. 8), the flow stress at 360 °C is only around 10% of the value at 20 °C. The output of the NN-based hardening function k_{NN} is normalized between [0.1, 2], as shown in Table 3. This NN hardening multiplier k_{NN} features a hyperbolic tangent function at the output layer. Consequently, the network output at 360 °C lies on the lower plateau of the $\tanh(\cdot)$ activation function, with minimum gradient to penalize upon. We therefore speculate that the mismatch is mainly caused by diminishing gradient effects during training. Extending the normalization range of the NN function k_{NN} to [0, 2] could potentially enhance the model performance at 360 °C.

The results from NT6 (Fig. 10), CH (Fig. 11) and SH (Fig. 12) simulations serve as validation data to assess the performance of the calibrated plasticity model. Similar to the NT20 training data, the worst predictions for NT6 and CH experiments (validation data) are observed for low speeds at 360 °C.

The SH simulations (Fig. 12) follow closely the experimental data points at the onset of yielding. Deviations between the experimental and the FE results are observed at large deformation. Specifically, at 1.3×10^{-2} m/s, the FE simulations tend to over-estimate the force towards the end of the curve. At 2.5 m/s, the FE simulations lie well within the experimental scatter, with a significant force drop caused by the temperature rise. We speculate that the Taylor-Quinney coefficient might be lower for the shear stress state which would reduce the temperature estimates for SH specimens.

Fig. 14 shows the surface temperature field before the onset of fracture for the intermediate speed (1.3×10^{-2} m/s) experiments starting at 180 °C. On average, the plastic dissipation leads to a temperature rise of approximately 20 °C, with a max 6 °C difference on the terminal temperature between the IR measurements and the FE simulations (CH case). It should be noted that the slight gradient in the experimental measurements (less than 4 °C) is observed along the horizontal axis of the specimen. This is attributed to the off-axis positioning of the infrared camera by around 30° (which was inevitable in our experimental setup).

Fig. 15 provides a 3D visualization of the NN based hardening function for selected temperatures and strain rates, respectively. The red lines in Fig. 15a–b highlight the material response at 20° and quasi-static strain rate (0.001/s). Comparing Fig. 15a,c,e,g, the flow stress reduces with the increase in temperature, i.e. the so-called temperature softening effect. At 20 °C (Fig. 15a), the isolines are mainly aligned along the strain rate axis, meaning that strain hardening is the dominant material response. This is in stark contrast to the results at 300 °C (Fig. 15g), where the isolines are primarily aligned along the plastic strain axis, indicating a strain rate dominant material response. The flow stress also rises with the increase of the strain rate (compare surfaces in Fig. 15b,d,f,h). This corresponds to a positive strain rate sensitivity across all temperatures.

5.3. Loading paths to fracture

The loading paths to fracture are critical in calibrating fracture initiation models, as they capture the loading history of the material point from the beginning of plastic deformation to the initiation of ductile fracture. We make use of a hybrid experimental-numerical approach to determine the loading paths [84]. They are extracted from the element in which the onset of fracture occurs, i.e. the element with the highest equivalent plastic strain in the finite element simulations.

In this study, the loading paths to fracture describe the evolution of five variables: (i) stress triaxiality η , (ii) Lode angle parameter $\bar{\theta}$, (iii) equivalent plastic strain $\bar{\epsilon}_p$, (iv) equivalent plastic strain rate $\dot{\bar{\epsilon}}_p$ and (v) temperature T . The 3D general stress state is characterized by the stress triaxiality η and the Lode angle parameter $\bar{\theta}$, calculated from the stress tensor invariants $\{I_1, J_2, J_3\}$:

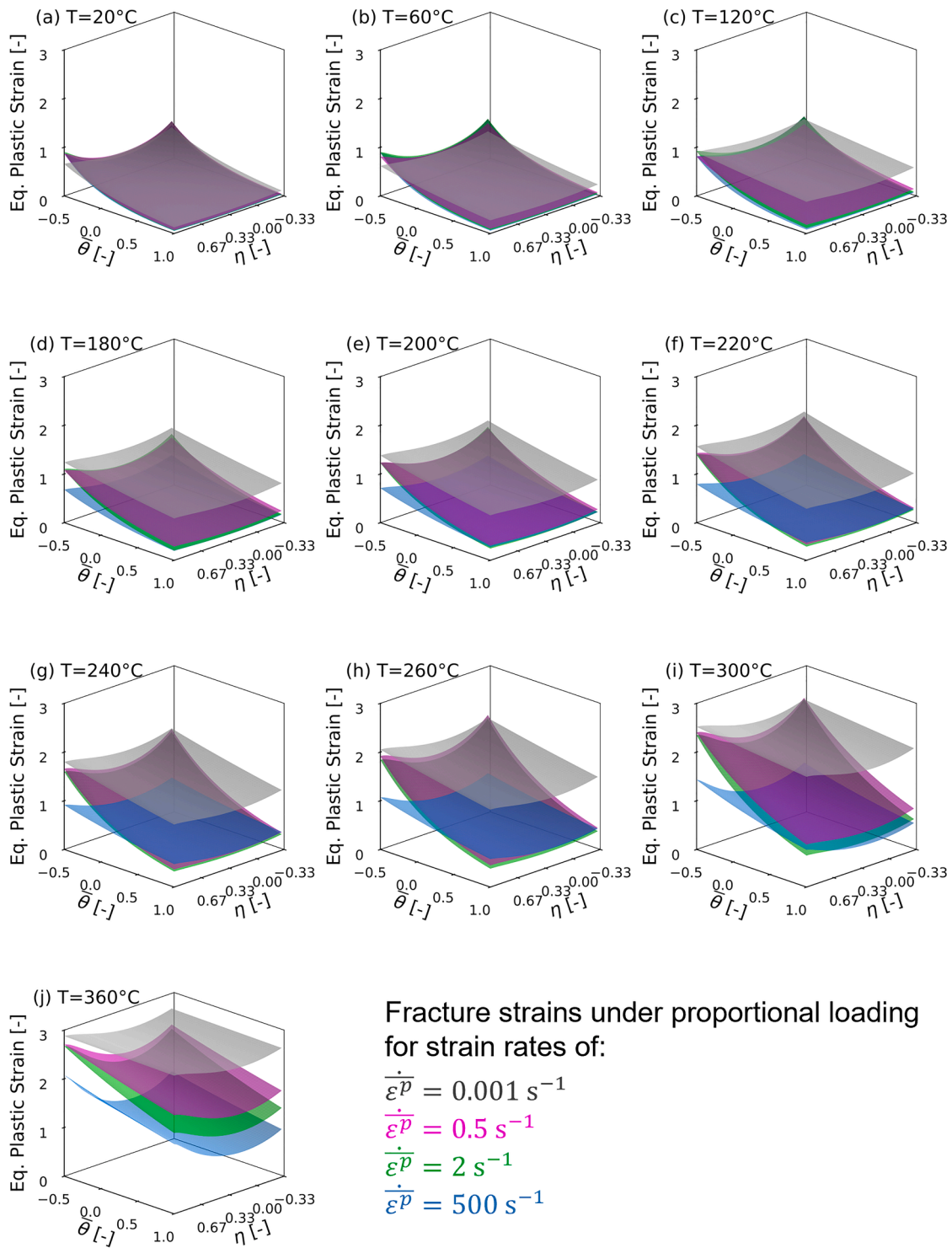


Fig. 24. Fracture strain under proportional loading for temperatures of 20 to 360 °C. The fracture loci for constant strain rates of 0.001/s, 0.5/s, 2/s and 500/s are highlighted in gray, magenta, green and blue respectively.

$$\eta = \frac{p}{\sigma_{VM}} = \frac{I_1}{3\sqrt{3}J_2} \tag{33}$$

$$\bar{\theta} = 1 - \frac{2}{\pi} \arccos \left[\frac{3\sqrt{3}}{2} \frac{J_3}{(J_2)^{3/2}} \right] \tag{34}$$

Most of the extracted loading paths are non-proportional, meaning that stress state, strain rate and temperature change throughout each experiment before fracture initiates (Figs. 16–19). These path

characteristics are primarily caused by adiabatic heating and changes in the gage section geometry due to large deformation.

At a first glance, for most specimens and testing speeds, the fracture strain decreases with the strain rate, while it increases with the temperature. Fig. 16 summarizes the evolution of the equivalent plastic strain as a function of the stress triaxiality. The results for slow, Int I, Int II and fast loading speeds are shown in black, magenta, green and blue color, respectively. The markers highlight the onset of fracture at the end of each loading path. Fig. 17 plots the evolution of the equivalent plastic

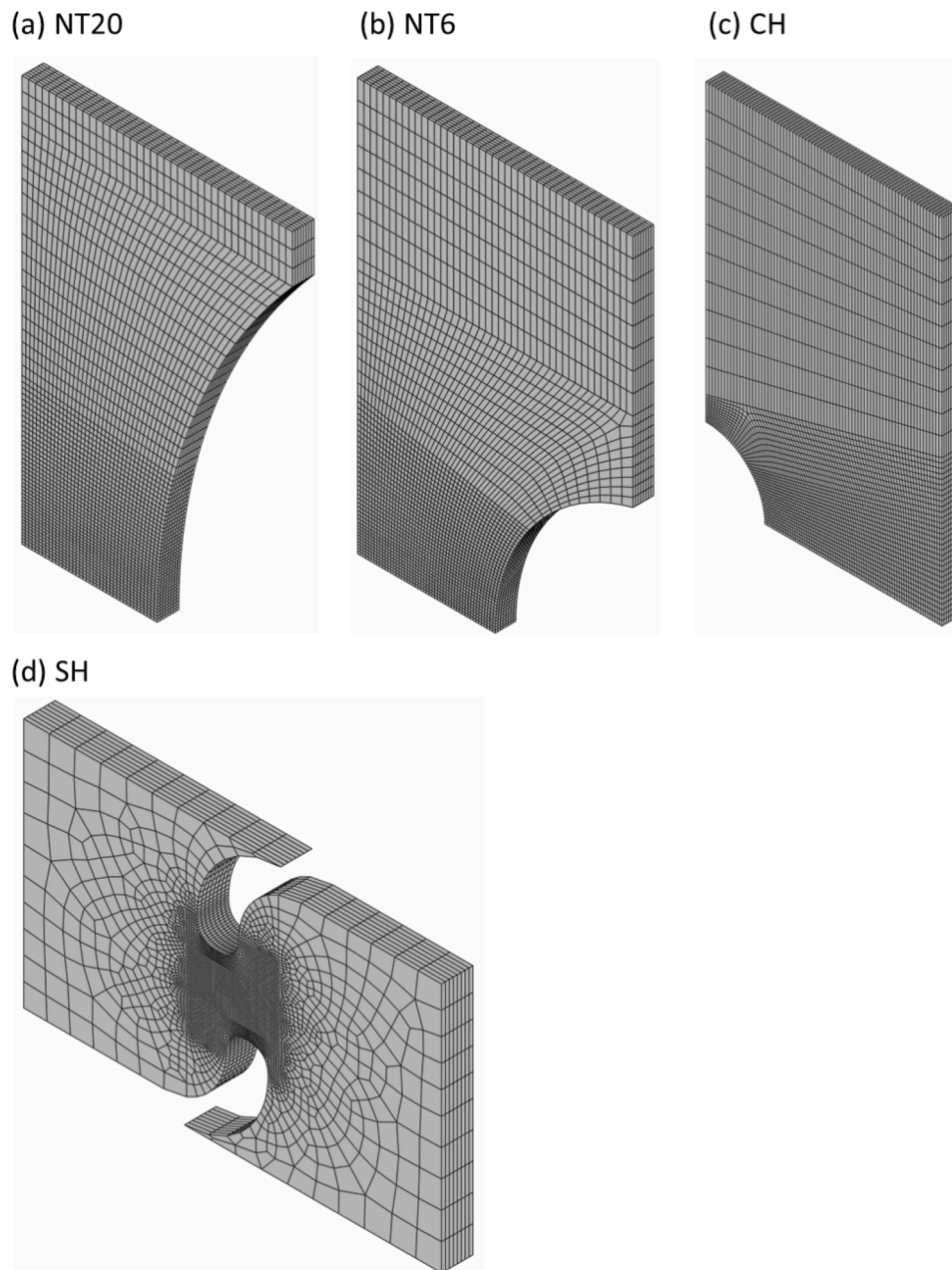


Fig. A 1. Finite element meshes as used for network training and validation (a) NT20, (b) NT6, (c) CH and (d) SH specimens.

strain as a function of Lode angle parameter in the same color scheme. For all temperatures investigated, experiments at low strain rates feature the highest fracture strain. The largest difference (65%) between the low-speed tests and the rest of the speeds is observed at 180 °C in the NT20 specimens. An increase in the temperature also leads to a higher fracture strain. The 360 °C experiments fail at strains above 2.5 (CH specimens), approximately ten times higher than those at 20 °C (0.25).

Apart from evolving stress states, the loading paths feature non-constant strain rate and temperature histories. After the onset of localized necking, the local strain rate increases by approximately one order of magnitude from the nominal value. Fig. 18a,c,e,g show the equivalent plastic strain as a function of strain rate categorized by different specimen geometries. As an example, the Int II experiments start at the nominal loading speed of around 1/s and end at around 10/s.

The conversion of plastic work into heat leads to a temperature rise for intermediate and high strain rate experiments, as shown previously by the temperature fields (Fig. 14). The right column plots in Fig. 18

show the temperature evolution as a function of the equivalent plastic strain. In general, a higher testing speed correlates with a higher temperature rise. Focusing on the NT20 tests with initial temperature of 180 °C, the temperature rises are 0 °C (slow), 23 °C (Int I), 36 °C (Int II) and 61 °C (fast), respectively.

Fig. 19 visualizes the loading paths in the plane of equivalent plastic strain and temperature for (a) NT20, (b) NT6, (c) CH and (d) SH experiments. The gray curves in Fig. 19a represent the rate and temperature histories extracted from all elements on the mid-plane of the NT20 specimen. As the mid-plane elements had been used for training the hardening model, the gray area highlights the rate- and temperature-domain covered during plasticity model training.

5.4. Fracture model training and validation

For the NN-based fracture model, a preliminary training is carried out on the effect of the network size (hyperparameters) on the prediction

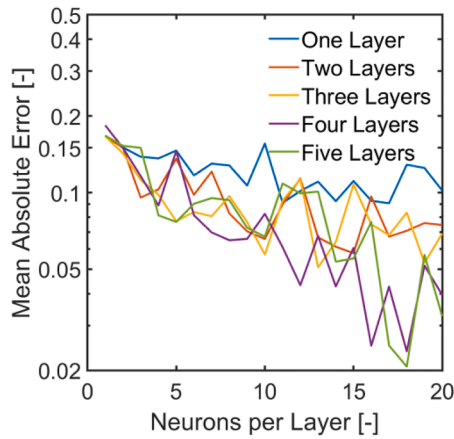


Fig. A 2. Performance of different network sizes using Adam optimizer. Adam achieves similar Loss values to RPROF, with less consistent performance for networks with many layers.

accuracy after 1000 epochs. All tested networks are initialized with the same random seeding. Fig. 20a summarizes the network performance as a function of its depth and width. Networks deeper than two layers show no significant increase in accuracy. For networks with more than ten neurons per layer only, a minor increase in accuracy is observed. We therefore settle for a network with two hidden layers of ten neurons, featuring in total $(2 + 1) \times 10 + (10 + 1) \times 10 + (10 + 1) \times 3 = 173$ trainable parameters (weights and biases).

The network is trained by minimizing the error on the terminal damage (Eq. 22). The training is stopped once the mean absolute error reaches a minimum and ceases to decrease (Fig. 20b). Combined with the clipping function (Eq. 32), this early stopping method successfully prevented over-fitting during network training. We achieve a mean absolute error on the terminal damage of 0.08 after 710 training epochs (corresponding to 9 h on a single core). Table 4 summarizes the normalization ranges of NN parameterized HC fracture model.

The plots in Figs. 21–22 summarize the prediction of the calibrated fracture model using full loading paths. The largest error on the damage prediction (0.52) is obtained for the NT20 specimen for “Int I” at 360 °C. This corresponds to a 0.78 (92%) difference on the predicted fracture strain. The NN predicts more accurate results below 260 °C, where 78 out of 98 samples feature damage error below 0.12. Below 260 °C, the maximum difference on fracture strain (0.19) is observed for the slow NT20 180 °C case.

5.5. Visualizations of the identified fracture model

The heart of the fracture model is the function $\bar{\epsilon}_f^p[\eta, \bar{\theta}, \dot{\bar{\epsilon}}_p, T]$ which describes the strain to fracture for hypothetical loading paths, along which the stress state, strain rate and temperature are kept constant. In the sequel, we visualize cross-sections of the above function in 2D and 3D sub-spaces. The fracture loci for plane stress conditions are plotted in dashed lines in Figs. 21–22 for strain rates of 0.001/s, 0.1/s, 2/s and 200/s. For all temperatures considered, the highest fracture strain is obtained for the low strain rate conditions (black dashed lines). The NN model also predicts a decreasing fracture strain for increasing strain rates which agrees with the conclusions drawn from the discussion of the loading paths in Section 5.3.

Pure shear (SH), uniaxial tension (UT), plane strain tension (PST) and equi-biaxial tension (EBT) are characteristic points of the fracture locus. For these stress states, we plot the plastic strain to fracture as a function of temperature and strain rates using the trained NN model (Fig. 23). As prescribed by the Hosford–Coulomb formulation (Eq. 18), the UT and EBT surfaces are identical, while the PST surface always features the lowest fracture strain. Across all four stress states, an

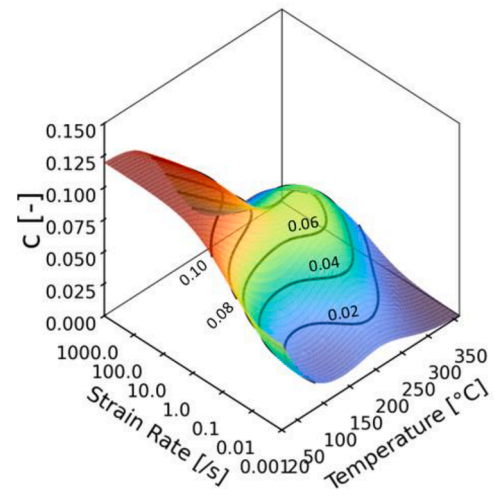
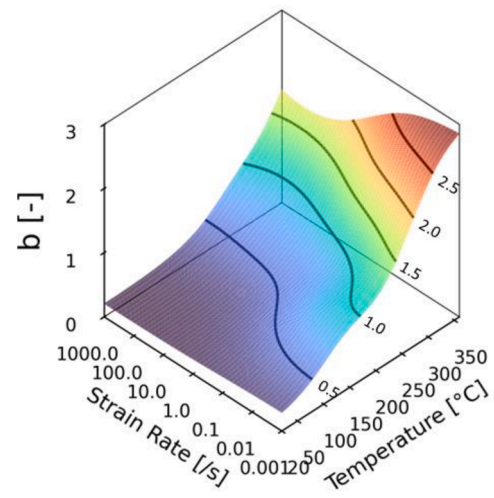
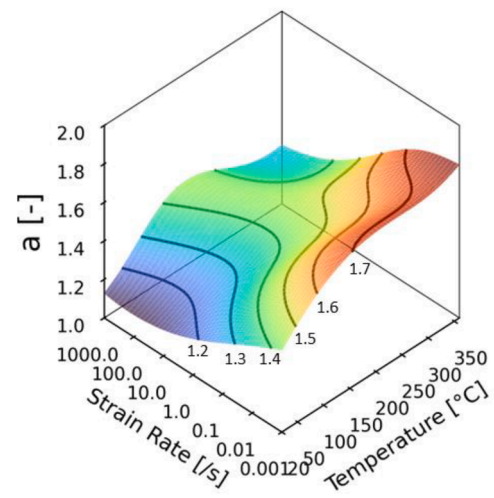


Fig. A 3. Evolution of Hosford–Coulomb *a*, *b*, *c* parameters as a function of the strain rate and temperature.

increase in the temperature leads to higher ductility (Fig. 23). A ductility peak is obtained around 350 °C at 0.001/s, with fracture strains as high as 2.7 for UT and EBT loadings. We also witness a lower fracture strain at higher strain rates, with a minimum in ductility obtained at 20 °C and 1000/s. Additionally, the Hosford–Coulomb fracture parameters {*a*, *b*, *c*} are visualized as a function of strain rate and temperature in Fig. A 3.

Ten selected temperatures and four selected strain rates of the calibrated NN fracture loci are shown in Fig. 24. All fracture surfaces follow the well-defined Hosford–Coulomb formulation, with different HC parameters given by the neural network. For most of the temperatures, an increase in the strain rate corresponds to a reduction in the fracture strain. The fracture loci feature a wider scatter at higher temperatures, indicating a higher strain rate sensitivity.

6. Conclusions

A combined experimental and numerical campaign on aluminum AA7075-T6 has been performed, covering temperatures from 20 °C to 360 °C and strain rates from 0.001/s to more than 100/s. The main findings are:

- The strain rate sensitivity of the hardening curve increases with the temperature. For example, increasing the strain rate from 0.001/s to 0.1/s corresponds to 0.3% stress increase at 20 °C, while at 180 °C this strain rate difference would lead to a 21% rise in the yield stress.
- A phenomenological plasticity model composed of a Yld2000-3D yield surface, an associated flow rule and a neural network based rate- and temperature-dependent hardening law can capture the large deformation response with good accuracy.
- The loading paths to fracture are determined by simulating experiments with 116 unique stress-state, strain rate and temperature combinations. The loading paths reveal evolving (non-constant) stress triaxiality, Lode angle parameter, strain rate, temperature, and equivalent plastic strain at the material point where fracture initiates.
- A new stress-state, strain rate-, temperature-dependent fracture initiation model is proposed to describe all hybrid numerical-experimental results. The backbone of the model is the stress-state dependent Hosford–Coulomb formulation which has been extended through a neural network term that accounts for the effects of strain-rate and temperature. The model is trained using a tailored back-propagation algorithm which accounts for the non-proportional and non-isothermal loading history of the experiments.

The proposed plasticity and fracture models are successfully validated through detailed finite element simulations of all experiments. The neural network formulation turned out to be particularly powerful to identify the effects of strain-rate and temperature from experiments with complex loading histories. Now that these effects have been revealed and quantified, the neural network formulation may also be approximated through simple parametric forms or replaced through tabulated models for immediate use in industrial practice.

CRedit authorship contribution statement

Xueyang Li: Conceptualization, Investigation, Data curation, Software, Visualization, Writing – original draft. **Christian C. Roth:** Conceptualization, Investigation, Writing – review & editing. **Dirk Mohr:** Funding acquisition, Project administration, Supervision, Visualization, Writing – review & editing.

Declaration of Competing Interest

The authors declare that they have no known competing financial interests or personal relationships that could have appeared to influence the work reported in this paper.

Data availability

No data was used for the research described in the article.

Acknowledgments

The authors would like to thank Prof. Nikos Karathanasopoulos (NYU/ETH), Prof. Vincent Grolleau (UBS/ETH) and Dr. Kedar S. Pandya (ETH) for their help with the experiments. Dr. Thomas Tancogne-Dejean (ETH) and Dr. Colin Bonatti (ETH) are thanked for valuable discussions. Thanks are also due to Mr. Julian N. Heidenreich (ETH) and Mr. Paul Meyer (ETH) for their help in programming, and Mr. Emmanouil Sakaridis (ETH) for help in post-processing.

Appendix

References

- [1] Korkolis YP, Kyriakides S. Path-dependent failure of inflated aluminum tubes. *Int J Plast* 2009;25:2059–80. <https://doi.org/10.1016/j.ijplas.2008.12.016>.
- [2] Fourmeau M, Borvik T, Benallal A, Hopperstad OS. Anisotropic failure modes of high-strength aluminum alloy under various stress states. *Int J Plast* 2013;48:34–53. <https://doi.org/10.1016/j.ijplas.2013.02.004>.
- [3] Roth CC, Mohr D. Ductile fracture experiments with locally proportional loading histories. *Int J Plast* 2016;79:328–54. <https://doi.org/10.1016/j.ijplas.2015.08.004>.
- [4] Roth CC, Mohr D. Determining the strain to fracture for simple shear for a wide range of sheet metals. *Int J Mech Sci* 2018;149:224–40. <https://doi.org/10.1016/j.jmecs.2018.10.007>.
- [5] Brünig M, Gerke S, Schmidt M. Damage and failure at negative stress triaxialities: experiments, modeling and numerical simulations. *Int J Plast* 2018;102:70–82. <https://doi.org/10.1016/j.ijplas.2017.12.003>.
- [6] Chen K, Scales M, Kyriakides S. Material response, localization and failure of an aluminum alloy under combined shear and tension: part II analysis. *Int J Plast* 2019;120:361–79. <https://doi.org/10.1016/j.ijplas.2019.04.002>.
- [7] Scales M, Chen K, Kyriakides S. Material response, localization, and failure of an aluminum alloy under combined shear and tension: part I experiments. *Int J Plast* 2019;120:340–60. <https://doi.org/10.1016/j.ijplas.2019.04.004>.
- [8] Marcadet SJ, Mohr D. Effect of compression-tension loading reversal on the strain to fracture of dual phase steel sheets. *Int J Plast* 2015;72:21–43. <https://doi.org/10.1016/j.ijplas.2015.05.002>.
- [9] Tvergaard V. Influence of voids on shear band instabilities under plane strain conditions. *Int J Fract* 1981;17:389–407. <https://doi.org/10.1007/BF00036191>.
- [10] Benzerga AA, Leblond JB. Ductile fracture by void growth to coalescence. In: *Advances in Applied Mechanics*. 44. Elsevier Inc; 2010. [https://doi.org/10.1016/S0065-2156\(10\)44003-X](https://doi.org/10.1016/S0065-2156(10)44003-X).
- [11] Dunand M, Mohr D. On the predictive capabilities of the shear modified Gurson and the modified Mohr–Coulomb fracture models over a wide range of stress triaxialities and Lode angles. *J Mech Phys Solids* 2011;59:1374–94. <https://doi.org/10.1016/j.jmps.2011.04.006>.
- [12] Liu ZG, Wong WH, Guo TF. Void behaviors from low to high triaxialities: transition from void collapse to void coalescence. *Int J Plast* 2016;84:183–202. <https://doi.org/10.1016/j.ijplas.2016.05.008>.
- [13] Morin D, Hopperstad OS, Benallal A. On the description of ductile fracture in metals by the strain localization theory. *Int J Fract* 2018;209:27–51. <https://doi.org/10.1007/s10704-017-0236-9>.
- [14] Luo T, Gao X. On the prediction of ductile fracture by void coalescence and strain localization. *J Mech Phys Solids* 2018;113:82–104. <https://doi.org/10.1016/j.jmps.2018.02.002>.
- [15] McClintock FA. A criterion for ductile fracture by the growth of holes. *J Appl Mech* 1968;35:363–71.
- [16] Rice JR, Tracey DM. On the ductile enlargement of voids in triaxial stress fields*. *J Mech Phys Solids* 1969;17:201–17. [https://doi.org/10.1016/0022-5096\(69\)90033-7](https://doi.org/10.1016/0022-5096(69)90033-7).
- [17] Gurson A.L. Continuum theory of ductile rupture by void nucleation and growth: part 1 — yield criteria and flow rules for porous ductile media 1977.
- [18] Tvergaard V, Needleman A. Analysis of the cup-cone fracture in a round tensile bar. *Acta Metall* 1984;32:157–69. [https://doi.org/10.1016/0001-6160\(84\)90213-X](https://doi.org/10.1016/0001-6160(84)90213-X).
- [19] Malcher L, Andrade Pires FM, César De Sá JMA. An extended GTN model for ductile fracture under high and low stress triaxiality. *Int J Plast* 2014;54:193–228. <https://doi.org/10.1016/j.ijplas.2013.08.015>.
- [20] Bai Y, Wierzbicki T. A new model of metal plasticity and fracture with pressure and Lode dependence. *Int J Plast* 2008;24:1071–96. <https://doi.org/10.1016/j.ijplas.2007.09.004>.
- [21] Lou Y, Huh H. Extension of a shear-controlled ductile fracture model considering the stress triaxiality and the Lode parameter. *Int J Solids Struct* 2013;50:447–55. <https://doi.org/10.1016/j.ijsolstr.2012.10.007>.
- [22] Lou Y, Yoon JW, Huh H. Modeling of shear ductile fracture considering a changeable cut-off value for stress triaxiality. *Int J Plast* 2014;54:56–80. <https://doi.org/10.1016/j.ijplas.2013.08.006>.
- [23] Mohr D, Marcadet SJ. Micromechanically-motivated phenomenological Hosford–Coulomb model for predicting ductile fracture initiation at low stress triaxialities.

- Int J Solids Struct 2015;67–68:40–55. <https://doi.org/10.1016/j.ijsolstr.2015.02.024>.
- [24] Xiao X, Mu Z, Pan H, Lou Y. Effect of the Lode parameter in predicting shear cracking of 2024-T351 aluminum alloy Taylor rods. Int J Impact Eng 2018;120:185–201. <https://doi.org/10.1016/j.ijimpeng.2018.06.008>.
- [25] Luo M, Dunand M, Mohr D. Experiments and modeling of anisotropic aluminum extrusions under multi-axial loading - Part II: ductile fracture. Int J Plast 2012;32–33:36–58. <https://doi.org/10.1016/j.jiplas.2011.11.001>.
- [26] Lou Y, Yoon JW. Anisotropic ductile fracture criterion based on linear transformation. Int J Plast 2017;93:3–25. <https://doi.org/10.1016/j.jiplas.2017.04.008>.
- [27] Li S, He J, Gu B, Zeng D, Xia ZC, Zhao Y, et al. Anisotropic fracture of advanced high strength steel sheets: experiment and theory. Int J Plast 2018;103:95–118. <https://doi.org/10.1016/j.jiplas.2018.01.003>.
- [28] Roth CC, Gary G, Mohr D. Compact SHPB system for intermediate and high strain rate plasticity and fracture testing of sheet metal. Exp Mech 2015;55:1803–11. <https://doi.org/10.1007/s11340-015-0061-x>.
- [29] Rahmaan T, Abedini A, Butcher C, Pathak N, Worswick MJ. Investigation into the shear stress, localization and fracture behaviour of DP600 and AA5182-O sheet metal alloys under elevated strain rates. Int J Impact Eng 2017;108:303–21. <https://doi.org/10.1016/j.ijimpeng.2017.04.006>.
- [30] Chatterjee A, Ghosh A, Moitra A, Bhaduri AK, Mitra R, Chakrabarti D. Role of hierarchical martensitic microstructure on localized deformation and fracture of 9Cr-1Mo steel under impact loading at different temperatures. Int J Plast 2018;104:104–33. <https://doi.org/10.1016/j.jiplas.2018.02.002>.
- [31] Johnson GR, Cook WH. A constitutive model and data for metals subjected to large strains, high strain rates and high temperatures. In: 7th international symposium on ballistics; 1983. p. 541–7.
- [32] Khan AS, Liang R. Behaviors of three BCC metal over a wide range of strain rates and temperatures: experiments and modeling. Int J Plast 1999;15:1089–109. [https://doi.org/10.1016/S0749-6419\(99\)00030-3](https://doi.org/10.1016/S0749-6419(99)00030-3).
- [33] Clausen AH, Borvik T, Hopperstad OS, Benallal A. Flow and fracture characteristics of aluminium alloy AA5083-H116 as function of strain rate, temperature and triaxiality. Mater Sci Eng A 2004;364:260–72. <https://doi.org/10.1016/j.msea.2003.08.027>.
- [34] Khan AS, Liu H. Strain rate and temperature dependent fracture criteria for isotropic and anisotropic metals. Int J Plast 2012;37:1–15. <https://doi.org/10.1016/j.jiplas.2012.01.012>.
- [35] Roth CC, Mohr D. Effect of strain rate on ductile fracture initiation in advanced high strength steel sheets: experiments and modeling. Int J Plast 2014;56:19–44. <https://doi.org/10.1016/J.JPLAS.2014.01.003>.
- [36] Huh H, Ahn K, Lim JH, Kim HW, Park LJ. Evaluation of dynamic hardening models for BCC, FCC, and HCP metals at a wide range of strain rates. J Mater Process Technol 2014;214:1326–40. <https://doi.org/10.1016/j.jmatprotec.2014.02.004>.
- [37] Wang J, Guo W-G, Li P, Zhou P. Modified Johnson-Cook description of wide temperature and strain rate measurements made on a nickel-base superalloy. Mater High Temp 2017;34:157–65. <https://doi.org/10.1080/09603409.2016.1252164>.
- [38] Chandran S, Liu W, Lian J, Münstermann S, Verleysen P. Strain rate dependent plasticity and fracture of DP1000 steel under proportional and non-proportional loading. Eur J Mech A/Solids 2022;92:104446. <https://doi.org/10.1016/j.euromechsol.2021.104446>.
- [39] Zerilli FJ, Armstrong RW. Dislocation-mechanics-based constitutive relations for material dynamics calculations. J Appl Phys 1987;61:1816–25. <https://doi.org/10.1063/1.338024>.
- [40] Follansbee PS, Kocks UF. A constitutive description of the deformation of copper based on the use of the mechanical threshold stress as an internal state variable. Acta Met 1988;36:81–93. [https://doi.org/10.1016/0001-6160\(88\)90030-2](https://doi.org/10.1016/0001-6160(88)90030-2).
- [41] Liang R, Khan AS. A critical review of experimental results and constitutive models for BCC and FCC metals over a wide range of strain rates and temperatures. Int J Plast 1999;15:963–80.
- [42] Abed FH, Voyiadjis GZ. A consistent modified Zerilli-Armstrong flow stress model for BCC and FCC metals for elevated temperatures. Acta Mech 2005;175:1–18. <https://doi.org/10.1007/s00707-004-0203-1>.
- [43] Rusinek A, Zaera R, Klepaczko JR. Constitutive relations in 3-D for a wide range of strain rates and temperatures - Application to mild steels. Int J Solids Struct 2007;44:5611–34. <https://doi.org/10.1016/j.ijsolstr.2007.01.015>.
- [44] Durrenberger L, Klepaczko JR, Rusinek A. Constitutive modeling of metals based on the evolution of the strain-hardening rate. J Eng Mater Technol 2007;129:550. <https://doi.org/10.1115/1.2772327>.
- [45] Abed F, Makarem F. Comparisons of constitutive models for steel over a wide range of temperatures and strain rates. J Eng Mater Technol 2012;134:021001. <https://doi.org/10.1115/1.4006171>.
- [46] Kajberg J, Sundin KG. Material characterisation using high-temperature Split Hopkinson pressure bar. J Mater Process Technol 2013;213:522–31. <https://doi.org/10.1016/j.jmatprotec.2012.11.008>.
- [47] Dunand M, Mohr D. Predicting the rate-dependent loading paths to fracture in advanced high strength steels using an extended mechanical threshold model. Int J Impact Eng 2017;108:272–85. <https://doi.org/10.1016/j.ijimpeng.2017.02.020>.
- [48] Conrad H. Thermally activated deformation of metals. JOM 1964;16:582–8. <https://doi.org/10.1007/BF03378292>.
- [49] Kocks UF, Argon AS, Ashby MF. Thermodynamics and kinetics of slip. Oxford ; London ; Edinburg ; New York ; Toronto: Pergamon Press; 1975.
- [50] Chu X, Leotoing L, Guines D, Ragneau E. Temperature and strain rate influence on AA5086 forming limit curves: experimental results and discussion on the validity of the M-K model. Int J Mech Sci 2014;78:27–34. <https://doi.org/10.1016/j.ijmecsci.2013.11.002>.
- [51] Mirfalah-Nasiri SM, Basti A, Hashemi R. Forming limit curves analysis of aluminum alloy considering the through-thickness normal stress, anisotropic yield functions and strain rate. Int J Mech Sci 2016;117:93–101. <https://doi.org/10.1016/j.ijmecsci.2016.08.011>.
- [52] Curtze S, Kuokkala VT. Dependence of tensile deformation behavior of TWIP steels on stacking fault energy, temperature and strain rate. Acta Mater 2010;58:5129–41. <https://doi.org/10.1016/j.actamat.2010.05.049>.
- [53] Jung IC, De Cooman BC. Temperature dependence of the flow stress of Fe-18Mn-0.6C-xAl twinning-induced plasticity steel. Acta Mater 2013;61:6724–35. <https://doi.org/10.1016/j.actamat.2013.07.042>.
- [54] Shen F, Münstermann S, Lian J. An evolving plasticity model considering anisotropy, thermal softening and dynamic strain aging. Int J Plast 2020;132:102747. <https://doi.org/10.1016/j.jiplas.2020.102747>.
- [55] Borvik T, Hopperstad OS, Berstad T, Langseth M. A computational model of viscoplasticity and ductile damage for impact and penetration. Eur J Mech A/Solids 2001;20:685–712. [https://doi.org/10.1016/S0997-7538\(01\)01157-3](https://doi.org/10.1016/S0997-7538(01)01157-3).
- [56] Erice B, Pérez-Martín MJ, Gálvez F. An experimental and numerical study of ductile failure under quasi-static and impact loadings of Inconel 718 nickel-base superalloy. Int J Impact Eng 2014;69:11–24. <https://doi.org/10.1016/j.ijimpeng.2014.02.007>.
- [57] Gorji MB, Mozaffar M, Heidenreich JN, Cao J, Mohr D. On the potential of recurrent neural networks for modeling path dependent plasticity. J Mech Phys Solids 2020;143:103972. <https://doi.org/10.1016/j.jmps.2020.103972>.
- [58] Bonatti C, Mohr D. One for all: universal material model based on minimal state-space neural networks. Sci Adv 2021;7:1–9. <https://doi.org/10.1126/sciadv.abf3658>.
- [59] Al-Haik MS, Hussaini MY, Garmestani H. Prediction of nonlinear viscoelastic behavior of polymeric composites using an artificial neural network. Int J Plast 2006;22:1367–92. <https://doi.org/10.1016/j.jiplas.2005.09.002>.
- [60] Talebi-Ghadikolae H, Moslemi Naeini H, Talebi-Ghadikolae E, Mirnia MJ. Predictive modeling of damage evolution and ductile fracture in bending process. Mater Today Commun 2022;31:103543. <https://doi.org/10.1016/j.mtcomm.2022.103543>.
- [61] Kessler BS, El-Gizawy AS, Smith DE. Incorporating neural network material models within finite element analysis for rheological behavior prediction. J Press Vessel Technol 2007;129:58–65. <https://doi.org/10.1115/1.2728894>.
- [62] Jenab A, Sari Sarraf I, Green DE, Rahmaan T, Worswick MJ. The use of genetic algorithm and neural network to predict rate-dependent tensile flow behaviour of AA5182-sheets. Mater Des 2016;94:262–73. <https://doi.org/10.1016/j.matdes.2016.01.038>.
- [63] Jordan B, Gorji MB, Mohr D. Neural network model describing the temperature- and rate-dependent stress-strain response of polypropylene. Int J Plast 2020;135:102811. <https://doi.org/10.1016/j.jiplas.2020.102811>.
- [64] Li X, Roth CC, Mohr D. Machine-learning based temperature- and rate-dependent plasticity model: application to analysis of fracture experiments on DP steel. Int J Plast 2019;118:320–44. <https://doi.org/10.1016/j.jiplas.2019.02.012>.
- [65] Li X, Roth CC, Bonatti C, Mohr D. Counterexample-trained neural network model of rate and temperature dependent hardening with dynamic strain aging. Int J Plast 2022;151:103218. <https://doi.org/10.1016/j.jiplas.2022.103218>.
- [66] Pandya KS, Roth CC, Mohr D. Strain rate and temperature dependent fracture of aluminum alloy 7075: experiments and neural network modeling. Int J Plast 2020;135:102788. <https://doi.org/10.1016/j.jiplas.2020.102788>.
- [67] Soares GC, Hokka M. Synchronized full-field strain and temperature measurements of commercially pure titanium under tension at elevated temperatures and high strain rates. Metals (Basel) 2022;12. <https://doi.org/10.3390/met12010025>.
- [68] Omer K, Abolhasani A, Kim S, Nikdejad T, Butcher C, Wells M, et al. Process parameters for hot stamping of AA7075 and α -7xxx to achieve high performance aged products. J Mater Process Technol 2018;257:170–9. <https://doi.org/10.1016/j.jmatprotec.2018.02.039>.
- [69] Wang X, Qiu Y, Slattery SR, Fang Y, Li M, Zhu SC, et al. A massively parallel and scalable multi-CPU material point method. ACM Trans Graph 2020;39. <https://doi.org/10.1145/3386569.3392442>.
- [70] Xiao W, Wang B, Zheng K. An experimental and numerical investigation on the formability of AA7075 sheet in hot stamping condition. Int J Adv Manuf Technol 2017;92:3299–309. <https://doi.org/10.1007/s00170-017-0419-6>.
- [71] Standard Astm. E112-12: standard test methods for determining average grain size. ASTM Int 2012;1–27. <https://doi.org/10.1520/E0112-12.1.4>. E112-12.
- [72] Grolleau V, Roth CC, Lafilé V, Galpin B, Mohr D. Loading of mini-Nakazima specimens with a dihedral punch: determining the strain to fracture for plane strain tension through stretch-bending. Int J Mech Sci 2019;152:329–45. <https://doi.org/10.1016/j.ijmecsci.2019.01.005>.
- [73] Dunand M, Maertens AP, Luo M, Mohr D, Dunand M, Mohr D. Experiments and modeling of anisotropic aluminum extrusions under multi-axial loading - Part I: plasticity. Int J Plast 2012;36:34–49. <https://doi.org/10.1016/j.jiplas.2012.03.003>.
- [74] Tancogne-Dejean T, Roth CC, Morgeneyer TF, Helfen L, Mohr D. Ductile damage of AA2024-T3 under shear loading: Mechanism analysis through in-situ laminography. Acta Mater 2021;205:116556. <https://doi.org/10.1016/j.actamat.2020.116556>.
- [75] Barlat F, Brem JC, Yoon JW, Chung K, Dick RE, Lege DJ, et al. Plane stress yield function for aluminum alloy sheets — part 1: theory. Int J Plast 2003;19:1297–319. [https://doi.org/10.1016/S0749-6419\(02\)00019-0](https://doi.org/10.1016/S0749-6419(02)00019-0).
- [76] Swift HW. Plastic instability under plane stress. J Mech Phys Solids 1952;1:1–18. [https://doi.org/10.1016/0022-5096\(52\)90002-1](https://doi.org/10.1016/0022-5096(52)90002-1).
- [77] Voce. The relationship between stress and strain for homogeneous deformations. J Inst Met 1948;74:537–62.

- [78] Gorji MB, Mohr D. Predicting shear fracture of aluminum 6016-T4 during deep drawing: combining Yld-2000 plasticity with Hosford–Coulomb fracture model. *Int J Mech Sci* 2018;137:105–20. <https://doi.org/10.1016/j.ijmecsci.2018.01.008>.
- [79] Logan RW, Hosford WF. Upper-bound anisotropic yield locus calculations assuming (111)-pencil glide. *Int J Mech Sci* 1980;22:419–30. [https://doi.org/10.1016/0020-7403\(80\)90011-9](https://doi.org/10.1016/0020-7403(80)90011-9).
- [80] Bishop C.M. Pattern recognition and machine learning. 2006. https://doi.org/10.1007/978-3-030-57077-4_11.
- [81] Rumelhart DE, Hinton GE, Williams RJ. Learning representations by back-propagating errors. *Nature* 1986;323:533–6. <https://doi.org/10.1038/323533a0>.
- [82] Riedmiller M, Braun H. A direct adaptive method for faster backpropagation learning: the RPROP algorithm. In: Proceedings of international conference on neural networks; 1993. p. 586–91. <https://doi.org/10.1109/ICNN.1993.298623>. 1993-January.
- [83] Kingma DP, Jimmy BA. Adam: A Method for Stochastic Optimization. Proceedings of the 3rd International Conference on Learning Representations (ICLR 2015). 2015. <https://doi.org/10.48550/arXiv.1412.6980>.
- [84] Dunand M, Mohr D. Hybrid experimental-numerical analysis of basic ductile fracture experiments for sheet metals. *Int J Solids Struct* 2010;47:1130–43. <https://doi.org/10.1016/j.ijsolstr.2009.12.011>.